

# Bar strengths in spiral galaxies estimated from 2MASS images

Eija Laurikainen, Heikki Salo

*Division of Astronomy, Dep. of Phys. Sci, FIN-90014, Finland*

## ABSTRACT

Non-axisymmetric forces are presented for a sample of 107 spiral galaxies, of which 31 are barred (SB) and 53 show nuclear activity. As a database we use JHK images from the 2 Micron All Sky Survey, and the non-axisymmetries are characterized by the ratio of the tangential force to the mean axisymmetric radial force field, following Buta & Block (2001). Bar strengths have an important role in many extra-galactic problems and therefore it is important to verify that the different numerical methods applied for calculating the forces give mutually consistent results. We apply both direct Cartesian integration and a polar grid integration utilizing a limited number of azimuthal Fourier components of density. We find that bar strength is independent of the method used to evaluate the gravitational potential. However, because of the distance dependent smoothing by Fourier decomposition the polar method is more suitable for weak and noisy images. The largest source of uncertainty in the derived bar strength appears to be the uncertainty in the vertical scale-height, which is difficult to measure directly for most galaxies. On the other hand, the derived bar strength is rather insensitive to the possible gradient in the vertical scale-height of the disk or to the exact model of the vertical density distribution, provided that a same effective vertical dispersion is assumed in all models. In comparison to the pioneering study by Buta & Block (2001), bar strength estimate is here improved by taking into account the dependence of the vertical scale-height on the Hubble type: we find that for thin disks bar strengths are stronger than for thick disks by an amount which may correspond to even one bar strength class.

We confirm the previous result by Buta & Block (2001) and Block et al. (2001) showing that the dispersion in bar strength is large among all the de Vaucouleurs's optical bar classes. In the near-IR 40 % of the galaxies in our sample have bars (showing constant phases in the  $m=2$  Fourier amplitudes in the bar region), while in the optical 1/3 of these bars are obscured by dust. Significant non-axisymmetric forces can be induced also by the spiral arms, generally in the outer parts of the galactic disks, which may have important implications on galaxy evolution. Possible biases of the selected sample are also studied: we find that the number of identified bars rapidly drops when the inclination of the galactic disk is larger than  $50^\circ$ . A similar bias is found in The Third Reference Catalogue of Bright Galaxies, which might be of interest when comparing bar frequencies at high and low redshifts.

**Key words:** galaxies: spiral – galaxies: active – galaxies: statistics – galaxies: kinematics and dynamics

## 1 INTRODUCTION

Bars consist mostly of old stellar population (de Vaucouleurs 1955; Elmegreen & Elmegreen 1985), which stresses their significance as dynamically important components in galaxies. In fact, a large fraction of galaxies have bars (Block & Wainscoat 1991; Knapen et al. 2000; Eskridge et al. 2000, Block et al. 2001), indicating that they must be long-lived phenomena in galaxies. Bars are fundamental in galaxy evolution, suggested to be driving forces for star formation, formation of rings and global spiral density waves, and even for the onset of nuclear activity. When quantified the correlations between bar strength and the other properties of the galaxies can be studied. The wavelength that best traces the dynamical mass is the near-IR, where the obscuration of dust is also less significant than in the optical region. For example, galaxies like NGC 5195, which are irregular in the optical may have regular grand-design spiral arms in the near-IR (Block et al. 1994), which emphasizes the importance of a new, more dynamical picture of the morphological structure in galaxies. A step toward that direction is the new dust penetrated classification of spiral arms in the near-IR (Block & Puerari 1999; Buta & Block 2001; Block et al. 2001), in which bar strength plays an important role.

As discussed by Buta & Block (2001; BB from hereon) there are many quantitative parameters which can be used to estimate bar strengths, such as bar-interarm contrast (Elmegreen & Elmegreen 1985) or light remaining after the disk and bulge components are subtracted (Seigar & James 1998). The most commonly used method is the maximum ellipticity of a bar, an approach justified by the analytical models by Athanassoula (1992), who showed that the non-axisymmetric forces in the bar correlate with the bar ellipticity. This method has been recently refined by Abraham & Merrifield (2000), who consider both the inner and outer contours of the image to better resolve the ellipticity of a bar. However, the ellipticity is not a full description of bar strength. In fact, a more physical approach has been taken by BB who estimate bar torques by calculating tangential forces in the bar region, taking into account also the underlying axisymmetric potential. Indeed, when refined, the bar torque method is probably the most promising way of estimating bar strengths.

When the bar torque method is finely tuned, future refinements will include the complex bar structures seen in many galaxies; taking more properly into account the vertical scale heights and their gradients, as well as taking into account bulge stretch scenarios upon deprojection of the images. In the bar torque method there are also different ways of evaluating the gravitational potential and it is important to verify that the different methods give mutually consistent results. For example, BB used the 2D Cartesian integration method by Quillen et al. (1994), whose new contribution in the potential evaluation was that the vertical density profile of the disk was taken into account in the convolution function. The potential was calculated in Cartesian grid by applying Fast Fourier Transform techniques (see also Elmegreen et al. 1989). On the other hand, in our study of IC 4214 (Salo et al. 1999) we evaluated the barred potential by first “smoothing” the image by calculating the Fourier decomposition of the surface density in a polar grid. In principle these two methods should give similar results.

In the present study bar strengths are calculated in JHK-bands for 107 spiral galaxies using the polar method (Salo et al. 1999) for the evaluation of the gravitational potential. The method has been improved by taking into account the recent observational work showing that bars in early-type galaxies are thicker than in late-type galaxies. Also, the effects of a distance dependent scale height, detected in many boxy/peanut shaped disks, are estimated. The algorithm of calculating forces is described, the different ways of estimating the gravitational potential are compared and Fourier analysis is applied for the analysis of bars. Also, biases of the sample are studied and the distributions of bar torques among the de Vaucouleurs’s optical bar classes are compared. In future the method will be further developed to better take into account the observational properties of bars and bulges in galaxies. The measurements of this paper have been used in comparisons of bar strengths between active and non-active galaxies by Laurikainen et al. (2002).

## 2 THE SAMPLE SELECTION

A sample of spiral galaxies was selected from the Third Reference Catalogue of Bright Galaxies (de Vaucouleurs et al. 1991, RC3) requiring that  $B_T < 12.5$  mag,  $cz < 2500$  km s<sup>-1</sup> and the inclination  $INC < 67^\circ$ . As a database we use the 2 Micron All Sky Survey (2MASS). As only about 50 % of the galaxies in our original sample have images available in 2MASS, the sample in the present form is not magnitude-limited. Some of the weakest images were also eliminated, because bar strengths could not be measured in a reliable manner for them. The final sample consists of 107 spiral galaxies, of which 31 are barred (SB) in RC3, 53 show nuclear activity, 42 are early-type spirals (SO/a-Sb) and the rest of the galaxies belong to late-types. To active galaxies we include Seyferts, LINERs and HII/Starburst galaxies, the type of activity being taken from NASA/IPAC Extra-galactic Database (NED), where the most recent classifications are available.

The frequency of bars in our sample is typical in comparison to other samples of galaxies. Including to barred galaxies both SB and SAB types we find a bar frequency of 62 %, which is similar to that obtained by Sellwood & Wilkinson (1993) for field galaxies (60 % barred) and by Ho et al. (1997) for a magnitude-limited sample ( $B_T < 12.5$ ) of spiral galaxies (59 % barred). A somewhat larger fraction of barred galaxies has been found by Hunt & Malkan (1999) for a sample selected by 12  $\mu$ m radiation (69 % barred) and by Moles et al. (1995) for a magnitude-limited sample extending to  $B_T = 13$  mag (68 % barred). The numbers of SB and SAB galaxies in our sample are rather similar (29 % and 33 %). While identifying bars in

the near-IR by Fourier techniques (see Section 5.3) the fraction of barred galaxies was found to be 40 %.

The fraction of SB galaxies among Seyferts and LINERs in our sample is 30 %, being similar as for the whole sample, in agreement with the bar fractions detected in the samples by Ho et al. (1997) and Mulchaey & Regan (1997). An enhanced frequency of bars is generally associated to HII/Starburst galaxies, for example, the fraction of SB-galaxies among the Markarian Starburst galaxies is even 75 % (Hunt & Malkan 1999). The bar fraction among HII/Starburst galaxies somewhat decreases when weaker nuclear star formation activity is considered: namely, in the whole  $12\ \mu\text{m}$  sample by Hunt & Malkan the fraction of SB-galaxies is 53 %, but while concentrating to smaller distances ( $cz < 5000\ \text{km s}^{-1}$ ), it decreases to 46 %. In our sample only 2 out of 17 HII-galaxies are classified as SB, which can be partly understood by the small distances of the galaxies ( $\langle cz \rangle = 1200\ \text{km s}^{-1}$ ): most probably we are picking the lower end of the nuclear HII-luminosity function, where bars may not be the driving forces for nuclear star formation.

The frequency of active nuclei in galaxy samples depends strongly on the redshift range studied: at small distances almost all galaxies show nuclear activity in some level (Ho et al. 1997), while the number of strong active nuclei increases with redshift. In our sample 53 % of the galaxies have active nuclei in terms of Seyferts, LINERs and HII/Starburst galaxies. As we have the same apparent magnitude limit as Ho et al., more HII/Starburst galaxies would be expected. The reason why we don't have more HII/Starburst galaxies most probably is that NED may not sample well the lowest level activity. The morphological types of Seyferts and LINERs in our sample are peaked to Sab galaxies, which is between the mean morphological types for Seyfert 1 (Sa) and Seyfert 2 (Sb) galaxies (Malkan et al. 1998), whereas 3/4 of the non-active galaxies belong to late Hubble types.

### 3 EVALUATION OF THE GRAVITATIONAL POTENTIAL

Like in BB, also here the bar strengths are estimated from the magnitude of the non-axisymmetric gravitational perturbation in comparison to the mean axisymmetric radial force field. For each radius  $r$  and azimuth  $\phi$  we calculate the tangential force  $F_T = \frac{1}{r}\partial\Phi/\partial\phi$  and the radial force  $F_R = \partial\Phi/\partial r$ , and define the relative strength of the perturbation as

$$Q_T(r) = F_T^{\text{max}}(r) / \langle F_R(r) \rangle, \quad (1)$$

where the average of radial force over azimuth is taken. Following BB the tangential force maxima were calculated separately in four quadrants of the image and the mean of these in each distance is used as the maximum  $F_T$ . In order to obtain a single measure for the strength we use  $Q_b$ , which is the maximum  $Q_T$  in the bar region. The radial distance where this maximal perturbation takes place is denoted by  $r_{Qb}$ .

For the force calculation the gravitational potential  $\Phi$  in the bar region must be evaluated. We assume that the surface density  $\Sigma$  is proportional to the surface brightness obtained from the near-IR image, and that the vertical density distribution follows a model profile  $\varrho_z(z)$ , normalized to unity when integrated over  $z$ . First it was assumed that the  $z$ -dependence of the mass density obeys the same formula everywhere in the galaxy (see Section 4.1), in which case the gravitational potential in the central plane of the galaxy can be written as (e.g. Quillen et al. 1994)

$$\Phi(x, y, z = 0) = -G \int_{-\infty}^{\infty} \int_{-\infty}^{\infty} \Sigma(x', y') g(x - x', y - y') dx' dy' \quad (2)$$

where the integral over  $z$ -direction is included to the convolution function  $g(x - x', y - y') \equiv g(\Delta r)$ , with  $\Delta r^2 = (x - x')^2 + (y - y')^2$ , defined as

$$g(\Delta r) = \int_{-\infty}^{\infty} \varrho_z(z) (\Delta r^2 + z^2)^{-1/2} dz. \quad (3)$$

Several models for  $\varrho_z(z)$  were applied, including the exponential model with scale-height  $h_z$ ,

$$\varrho_z(z) = \frac{1}{2h_z} \exp(-|z/h_z|), \quad (4)$$

and the often used isothermal sheet model (van der Kruit & Searle 1981),

$$\varrho_z(z) = \frac{1}{2h_{\text{sech}2}} \text{sech}^2(z/h_{\text{sech}2}), \quad (5)$$

where  $h_{\text{sech}2}$  is the isothermal scale-height. Usually, when isothermal model is used,  $h_{\text{sech}2}$  is set equal to  $2h_z$ , to yield a same slope at large  $z$  as for the exponential model. According to van der Kruit (1988) galactic disks may, however, deviate from isothermal shape near the galactic plane, in which case a better approximation for the density distribution would be

$$\varrho_z(z) = \frac{1}{\pi h_{\text{sech}}} \text{sech}(z/h_{\text{sech}}). \quad (6)$$

In the case of *sech*-law, Barnaby & Thronson (1992) identify  $h_{\text{sech}}$  with  $(\pi/4)h_z$ , to get the same central plane density as in the *sech*<sup>2</sup>-law. However, in this study we briefly check *sech*-law with  $h_{\text{sech}} = h_z$ , in which case the slope of the vertical profile

corresponds to exponential model at large  $z$ . De Grijs et al. (1997) have explored a more general family of fitting functions, which include the above functions as special cases. As will be discussed below the adopted vertical model has rather little influence on the derived forces, provided that appropriately defined scale-heights are used.

In comparison to BB we use a somewhat different method for the evaluation of the gravitational potential, mainly because the 2MASS images used here have a more poor resolution ( $1''/\text{pix}$ ) and lower signal-to-noise (S/N) ratio than the images used by BB. Thus, instead of calculating the gravitational potential directly from the image pixels, the images are first “smoothed” by calculating the Fourier decompositions of the surface densities in different radial zones,

$$\Sigma(r, \phi) = \Sigma_0(r) + \sum_{m=1}^{m=\infty} \Sigma_m(r, \phi) = A_0(r) + \sum_{m=1}^{m=\infty} A_m(r) \cos [m(\phi - \phi_m(r))]. \quad (7)$$

The density of each Fourier component is then separately tabulated as a function of radius and azimuth, and for each density component the corresponding potential component is obtained by

$$\Phi_m(r, \phi, z=0) = -G \int_0^\infty r' dr' \int_0^{2\pi} \Sigma_m(r', \phi') g(\Delta r) d\phi', \quad (8)$$

with  $\Delta r^2 = r'^2 + r^2 - 2rr' \cos(\phi' - \phi)$ . The integration over azimuthal direction is carried out by Fast Fourier Transform (FFT), whereas in the radial direction a direct summation is used. An azimuthal offset of one half bin is used between density and potential locations, and the force components at density locations are obtained from the potential by numerical differentiation. For test purposes, we also applied Cartesian potential evaluation, solving Eq. (1) with 2D FFT as in BB. In comparison to direct Cartesian force evaluation the advantage of our polar method is that also rather weak and noisy structures can be measured in a reliable manner, due to the smoothing implied by Fourier decomposition. Also, it is possible to limit the density to even components, most likely to characterize the non-axisymmetry related to the bar. Our method also gives directly the different Fourier modes of the potential and force components, which are sometimes of interest.

Like in BB and Quillen et al. (1994), we made use of the fact that the convolution function  $g(\Delta r)$  can be numerically integrated and tabulated as a function of  $\Delta r/h$ ,  $h$  denoting the vertical scale-factor used, so that the integration over  $z$ -direction can be replaced by a much faster interpolation from pre-calculated tables. In addition, since in the polar method only the integration over azimuth is carried out by FFT, a distance-dependent  $h$  can be used: in this case  $g(\Delta r/h)$  in Eq. (8) remains cyclic with  $\phi' - \phi$  even if  $h = h(r')$ . In the Cartesian 2D FFT this can not be done as the convolution function needs to be cyclic in both  $x - x'$  and  $y - y'$ .

In Fig. 1 we display the convolution functions corresponding to various vertical models. The upper row shows the density profiles and convolution functions corresponding to exponential, *sech*, and *sech*<sup>2</sup>-model profiles. The difference in  $g(\Delta r)$  is significant only for  $\Delta r < h_z$ . In the lower row of the figure we illustrate the relative insensitiveness of  $g(\Delta r)$  for a wider range of  $\rho_z(z)$  models, including the Gaussian model,

$$\rho_z(z) = \frac{1}{\sqrt{2\pi}h_{gauss}} \exp\left(-\frac{z^2}{2h_{gauss}^2}\right), \quad (9)$$

and a uniform slab-model,

$$\rho_z(z) = \frac{1}{2h_{uni}}, \quad -h_{uni} < z < h_{uni}. \quad (10)$$

In order to make the models comparable, the scale factors in each case were chosen in a manner that yields the same vertical dispersion as the exponential model with  $h = h_z$ , namely  $\langle z^2 \rho_z(z) \rangle / \langle \rho_z(z) \rangle = 2h_z^2$ . In this case

$$h_{gauss}/h_z = \sqrt{2},$$

$$h_{sech2}/h_z = \sqrt{24}/\pi,$$

$$h_{sech}/h_z = \sqrt{8}/\pi, \quad (11)$$

$$h_{uni}/h_z = \sqrt{6}.$$

As expected, the more peaked the density profile is toward the central plane, the larger is the value of  $g(\Delta r)$  when  $z \rightarrow 0$ . In each case  $g(\Delta r) \propto 1/\Delta r$  for large  $\Delta r$ , while  $g(\Delta r)$  increases logarithmically when  $\Delta r \rightarrow 0$ . In the case of a uniform slab, analytical integration yields

$$g_{uni} = \frac{1}{h_{uni}} \log\left(\frac{h_{uni} + \sqrt{h_{uni}^2 + \Delta r^2}}{\Delta r}\right), \quad (12)$$

in agreement with the result of the numerical integration shown in Fig. 1. For comparison, Fig. 1 displays also the case of using 2-D softened gravity,

$$g_{soft} = 1/\sqrt{\Delta r^2 + \epsilon^2}, \quad \text{with } \epsilon^2 = 2h_z. \quad (13)$$

In conclusion, the convolution function depends very little on the model used for the vertical mass distribution as long as models with a same vertical dispersion are compared. In the next section bar strengths calculated using different vertical models are compared, as well as results obtained by the two different integration methods.

## 4 TESTING THE ALGORITHM

### 4.1 Polar vs. Cartesian integration

We next investigate our algorithms of force evaluation using NGC 1433 as a test case. For this galaxy Ron Buta has provided us with his high quality H-band image, with a 1.141 arcsec pixel scale (Buta et al. 2001). Fig. 2 compares our standard polar method, and our Cartesian potential evaluation, where the de-projected image is interpolated to a density array and then FFT in Cartesian coordinates is applied with a grid resolution ranging from  $64 \times 64$  to  $512 \times 512$ . In both polar and Cartesian cases the forces were calculated from a region with radius of  $r_{max} = 180$  pixels (205 arcsecs). According to Fig. 2 the obtained  $Q_T$ -profiles converge rapidly as more Fourier components are included, or when a finer Cartesian grid is used. The profiles obtained with the two methods also agree well: the maximum  $Q_T$  agrees within a few percent. The only differences appear at large  $r$ , where the polar method yields smaller  $Q_T$ . This is due to distance-dependent smoothing implied by the polar method, whereas in the Cartesian integration the maximum tangential forces for large  $r$  are mainly due to spurious values connected to individual image pixels. Thus, since the outer parts of the galaxy have a low S/N-ratio, the smoothing in the polar method is also physically well motivated.

As the polar method is based on calculating Fourier amplitudes for different density components, it is interesting to check how much each component contributes to the total force: in Fig. 2 even components up to  $m=10$  are studied. We have used an exponential vertical profile, both with  $h_r/h_z = 2.5$ , representing an early-type galaxy, and with  $h_r/h_z = 10$ , to study the effect of assuming a very flat disk. The density amplitudes  $m=2$  and  $m=4$  are known to be the strongest in bars, while in early-type galaxies the  $m=6$  and  $m=8$  may also be significant (Ohta 1996). For NGC 1433 (type Sb) the density amplitudes we find in H-band are fairly similar to those displayed for the I-band by Buta (1986), with  $A_2/A_0$  attaining a maximum  $\approx 0.97$  at  $r = 110''$ , and a secondary maximum of  $\approx 0.6$  at  $r \approx 50''$ . For  $m = 4, 6, 8, 10$  the maximum  $A_m/A_0$  are about 0.42, 0.22, 0.13, 0.09, respectively, and for the resulting force the maximum appears at  $r_{Qb} = 70''$ , which corresponds to about 90% of the bar radius ( $R_{bar} = 77''$ , Buta 1986). For  $h_r/h_z=2.5$  about 75% of the tangential force is due to the  $m=2$  density component, and with the inclusion of the  $m=4$  component  $Q_b$  increases to 97 % of its value obtained by including all even components up to  $m=10$ . However, for the case of a flatter galaxy the influence of higher order Fourier components would become somewhat more important: in the case of  $h_r/h_z = 10$ ,  $Q_b = 70\%, 90\%, 98\%$  of its maximum value, when including the density components up to  $m_{max} = 2, 4, 6$ , respectively. Thus even in this case the density components above  $m=6$  have fairly little influence. This difference in the relative importance of various Fourier components follows from the fact that planar density variations correspond to force variations only if their planar scale significantly exceeds  $h_z$ : smaller  $h_r/h_z$  thus suppresses the force variations corresponding to large  $m$ .

In the above example the calculation region covered well the optical disk of the galaxy, and the maximum  $Q_T$  was obtained at  $r_{max}/r_{Qb} \approx 3$ . However, in the case of 2MASS images the outer disks for distant galaxies are sometimes not deep enough. In order to check the influence of the size of calculation region, a series of integrations with decreasing  $r_{max}$  was conducted for NGC 1433. For  $r_{max}/r_{Qb} = 2$  the resulting value of  $Q_b$  was only about 2% smaller (no shift in  $r_{Qb}$ ), whereas for  $r_{max}/r_{Qb} = 1.5$  the reduction was already significant, amounting to 15%. About 2/3 of this reduction is due to reduced tangential force, while the remaining part comes from the overestimated radial force due to disk truncation. However, the location of  $Q_T$ -maximum was still fairly little affected ( $66''$  vs.  $70''$ ). All our subsequent force evaluations from 2MASS images are based on images covering a radius at least twice as large as the derived  $r_{Qb}$ .

We also checked the influence of different model functions for the vertical profile on NGC 1433 (Fig. 3). The models correspond to those studied in Fig. 1, each having the same vertical dispersion. As expected, based on the behavior of the convolution functions, a more centrally peaked vertical profile yields a slightly larger  $Q_b$ , although the shape of the  $Q_T$ -profile is little affected. For early-type galaxies with  $h_r/h_z = 2.5$ , the difference in  $Q_b$  between the exponential and uniform models is 15%, which is much less than the difference between the cases  $h_r/h_z = 2.5$  and  $h_r/h_z = 10$  for a fixed vertical model function. Also, while comparing more realistic vertical models, namely the exponential and the isothermal model,  $Q_b$  is affected only 5%. In general, when the vertical extent of the disk is reduced, the exact form of the vertical density law becomes less important. In the limit of very large  $h_r/h_z$  the difference between including 3D vertical profile and the use of softening in 2D force-evaluation becomes also small, in agreement with Salo et al. (1999). However, for large disk thicknesses ( $h_r/h_z = 2.5$ ), the use of softened gravity severely underestimates  $Q_b$ .

## 4.2 Distant dependent disk thickness

As many galaxies have boxy/peanut shaped structures, for which the vertical thickness has found to increase towards the outer parts of the galaxies, we also studied a case with distant dependent vertical scale-height. Radial distributions of  $Q_T$  were calculated for NGC 1433 using an exponential density model, when  $h_z$  was assumed to have a mean value and a gradient typical for early-type galaxies (see Section 5.1). As shown in Fig. 4 the vertical density gradient has a fairly small effect on bar strength: in comparison to the case where a constant  $h_z$  was assumed, a gradient of 0.05 in  $h_z$  affects  $Q_T$  at maximum only by 4%. In the figure three cases are demonstrated showing how the location of the mean vertical thickness affects  $Q_T$  measurement. In comparison to constant vertical scale-height, radially increasing  $h_z$  typically slightly reduces the derived bar strength. This is due to two competitive effects: on one hand the tangential force increases in the region where the vertical scale-height is reduced, but at the same time axisymmetric radial force is also increased in the same region (see Fig. 5).

In interacting galaxies gradients of the vertical scale-heights are generally larger than for normal galaxies, and contrary to normal galaxies, may also appear in late-type systems. Therefore we studied also some cases, where the  $h_z$  gradient was twice as large as for normal galaxies. For  $h_r/h_z=2.5$  the effect of the gradient on  $Q_b$  was still unimportant  $Q_b$  being reduced only by 3%. Thin disks were even more less affected: for  $h_r/h_z=10$  we found that while adding a gradient of 0.03,  $Q_b$  was maintained unchanged. We can safely conclude that the vertical scale-height gradient, typical for boxy/peanut shaped bars, does not significantly affect bar strength.

## 4.3 Comparison to BB

We next compare our results with those obtained by BB. Bar strengths for 13 galaxies in the sample by BB were calculated in H-band, using the same orientation parameters as used in BB (see Table 4). Also, following BB the vertical mass distribution was approximated by an exponential function with  $h_z = 325$  kpc, which is the scale-height of the disk in the Milky Way. As shown in Fig. 6, there is a small shift toward somewhat larger  $Q_b$  in our measurements, but generally the agreement between the two measurements is quite good. No softening was used in our potential evaluation. A possible cause of the small difference is that some form of additional gravity softening was included to the potential evaluation in BB, besides using a vertically extended density model. This possibility is suggested by the form of the convolution function  $g(r)$  shown in Fig. 2 in Quillen et al. (1994), being the method used by BB. In comparison to our  $g(r)$  (Fig. 1), their function seems to attain a constant value for  $\Delta r/h \rightarrow 0$ , much like our curve for softened gravity. Nevertheless, no explicit gravity softening was mentioned in Quillen et al., so it is not clear whether this is the cause for the difference. It is also worth noticing that the comparison was made using 2MASS images, many of which were of more poor quality than the images used by BB. In Table 4 we also show that the vertical density model barely affects the derived bar strength.

# 5 CALCULATION OF THE NON-AXISYMMETRIC FORCES FOR THE SAMPLE

## 5.1 Observed parameters in the potential evaluation

As discussed in the previous section, several approximations were made while calculating the gravitational potential, largely following BB. The main assumption was that the mass-to-luminosity ratio (M/L) is constant throughout the disk. This assumption was made for simplicity, because otherwise possible M/L- variations along the disk should be known for each individual galaxy. The studies of color gradients in galaxies have shown that the central regions of the disks are often redder than the outer disks, which actually suggests larger stellar M/L-ratios in the inner disks (Bell & de Jong 2001). Another indicator of a possible non-constancy of the M/L-ratio comes from the comparison of the optical surface photometry with the surface mass densities obtained from the rotation curves, showing that the M/L-ratio may vary along the disk (Takamiya & Sofue 2000). However, it is possible that the M/L-ratio is rather constant in the bar region (see Quillen et al. 1994), in which case the made assumption should be reasonably good.

In the evaluation of the barred potential a model for the vertical mass distribution was assumed. The most commonly used models are the exponential and isothermal functions, both being physically justified. An isothermal density function is expected if stars, once formed, do not interact with the other components of the galaxy. Stellar populations of different ages can then be understood as quasi-independent components with different velocity dispersions (Dove & Thronson, 1993) so that a more complete picture would be achieved by assuming a super-position of a large number of isothermal sheets with different  $h_z$  (Kujken 1991). On the other hand, if gas settles into an equilibrium prior to star formation or considerable heating of the disk has occurred during the life of a galaxy, an exponential density profile is expected (Burkhead & Joshii 1996). However, empirically the two functions are difficult to distinguish, because the density functions look similar at large vertical heights, whereas near to the galactic plane the evaluation of the density function is complicated by the effects of dust. For the vertical density distribution we used an exponential function. However, based on discussion in Section 4.1, the uncertainty in the vertical model function should have fairly small influence on derived forces.

For bar strength measurements, more critical is the thickness of the disk. It has been found to depend on the morphological type of the galaxy (de Grijs 1998) and also to correlate with the radial scale-length of the disk (Wainscoat et al. 1989; van

der Kruit 1988). For early-type galaxies we used  $h_r/h_z=2.5$ , and for late-type systems  $h_r/h_z=4.5$ . For  $h_r$  we use the optical V-band scale-lengths from Baggett et al. (1998), and if not available, they were estimated from the 2MASS images by us. Optical scale-lengths were used, but they are expected to be rather similar with those in the near-IR: namely using the bulge-to-disk decompositions given by de Jong (1996) for 186 spiral galaxies, we found that the scale-lengths in V-band deviate on the average only 5% from those in K-band. For three of the galaxies, pgc 10266, pgc 15821 and pgc 40097, the scale-lengths by Baggett et al. were judged unrealistic: for two of the galaxies they were rather measures of the brightness slopes in the bulge region, and for one galaxy the given scale-length represented the outermost very shallow part of the disk, while we are interested in the disk under the bar. Therefore, also for these three galaxies the scale-lengths were estimated from 2MASS images.

Bars and bulges have often rather complex structures and may in some cases be difficult to distinguish from each other. For example, 45 % of all galaxies (SO-Sd) may have boxy or peanut shaped bulges or bars, having vertical disk profiles that become thicker towards the outer parts of the disks (Lutticke et al. 2000, Schwarzkopf & Dettmar 2001). These gradients are pronounced in early-type galaxies, but generally do not appear in late-type galaxies. The boxy/peanut structures are often thought to be bulges, but recent observations rather support the idea that they more likely represent the thick parts of the bars. This interpretation is also supported by the simulations by Athanassoula (2002) who has shown that boxy/peanut structures are formed from the particles of the disks or bars during the evolution of the galaxy. In this work we have made the simplified assumption that  $h_z$  is constant throughout the disk, although the effect of the thickening of the disk toward the outer parts of the disk is also investigated. In the test we used a  $dh_z/dr$  gradient of 0.05, typical for normal SO/a galaxies (Schwarzkopf & Dettmar 2001). Galaxy interactions and mergers of small satellite galaxies can also be efficient in thickening the disk especially in the outer parts of the galaxies (Toth & Ostriker 1992; Walker et al. 1996). In fact, observations by Schwarzkopf & Dettmar have shown that the vertical heights of the disks for interacting galaxies can be twice as large as for non-interacting galaxies. Bulges were assumed to be as flat as the disks, which is also a simplified assumption, but may still be valid for the triaxial bulges of SB-galaxies (Kormendy 1982, 1993). Evidently, the treatment of bulges need to be improved in future.

## 5.2 Calculation of forces for sample galaxies

As a database JHK images of the 2MASS survey were used. The spatial resolution of the images was one arc second, and the image quality was generally best in the H-band. Our procedure of estimating the non-axisymmetric forces consisted of the following steps: (1) cleaned sky-subtracted mosaics were constructed, (2) galaxies were de-projected to face-on orientation, (3) the images were rebinned by a factor of two, (4) Fourier decomposition of the surface density was calculated, and barred potentials were evaluated using the even components up to  $m=6$ , (5) the tangential ( $F_T$ ) and the mean axisymmetric radial forces ( $\langle F_R \rangle$ ) were calculated, and finally (6) maps of the force ratios were constructed:

$$Q_T(r, \phi) = F_T(r, \phi) / \langle F_R(r, \phi) \rangle.$$

For a bar the map shows four well defined regions where the force ratio reaches a maximum or minimum around or near the end of the bar. As in BB, we call this structure as a “butterfly pattern”.

The field of view in the 2MASS images is relatively small and also a large fraction of the galaxies in our sample are quite nearby objects so that mosaics of 2-5 images were generally made. The image quality was not as good in the borders as in the central parts of the frames, which in principle could seriously affect the quality of the mosaics in the regions of interest. For the most nearby galaxies this was not a problem, because the S/N-ratio was high in all parts of the images. For the distant objects the problem was solved so that we never combined images if their borders appeared in the bar region or in the central parts of the galaxies. Before combining the images the over-scan regions were removed and the sky values given in the image headers were subtracted. The background levels of the frames were then refined to get similar count levels in the galaxy regions in the combined images. Positioning of the frames in the mosaics was done using stars common in the combined images. Finally the foreground stars and bad pixels were rejected.

The cleaned (mostly mosaics) images were de-projected to face-on orientation using the position angles (PA) and inclinations of the disks given in Table 1. In the table some other properties of the galaxies like the mean revised morphological type  $T_m$ , the blue apparent magnitude  $B_T$ , the type of nuclear activity, and the scale-length of the disk  $h_r$ , are also shown. The orientation parameters, the morphological types and the apparent magnitudes are from RC3 if not otherwise mentioned. For some of the galaxies, instead of using the orientation parameters from RC3, they were estimated from the Digitized Sky Survey Plates by us. For example, for pgc 18258 the surface brightness contours are clearly affected by the super-position of a small companion, which has not been taken into account in the orientation parameters in RC3. For the galaxies that had no estimation of PA in the literature, but the disks were in nearly face-on orientation, we used  $\text{INC}=0$ . In order to estimate properly the axisymmetric radial forces the bulges were not subtracted.

The maximum of non-axisymmetric forces,  $Q_b$ , and their radial distances,  $r_{Qb}$ , are shown in Tables 2 and 3, measured in J, H and K-bands. The uncertainties attached in the tables are the maximum deviations between the four image quadrants. However, the largest uncertainty (see Section 4.1) is due to the observed scatter in  $h_r/h_z$  within each morphological type,

which for example for Sc-galaxies induces an uncertainty of about 15 % in  $Q_b$ . Non-axisymmetric forces are also sensitive to the orientation parameters of the galaxies: BB estimated that an uncertainty of  $\pm 10$  % in the inclination and position angle can induce an uncertainty of two bar strength classes (one bar strength class corresponds to 0.1 units in  $Q_b$ ). Indeed, in future this work can be improved when accurate position angles and inclinations will be available for all of the galaxies studied. Especially for interacting galaxies the photometrical orientation parameters are generally determined from warped or distorted outer disks so that the kinematic observations for them give more reliable values. For example, for M51 the kinematically (Tully 1974) and photometrically (Spillar et al. 1992) estimated inclinations deviate by about  $20^\circ$ , and for IC 4214 by  $10^\circ$  (Buta et al. 1999), for which the difference can be explained by the bar potential (see Salo et al. 1999). On the other hand, the uncertainty caused by the vertical model (*exp* v.s. *sech*<sup>2</sup>) is negligible for thin disks and only about 5 % for thick disks. Also, the number of Fourier modes or the size of the measurement region do not affect  $Q_b$  significantly, if large enough measurement regions ( $r_{max} > 2r_{Qb}$ ) and enough Fourier modes (even modes up to  $m=6$ ) are used. The effect of the boxy/peanut shaped structures in terms of increasing vertical scale-height toward the outer parts of the disks also appeared to be insignificant for bar strength.

### 5.3 Identification of bars and calculation of bar ellipticity

Bars in the near-IR were identified by Fourier techniques. In distinction to bars in general, we call “classical bars” the morphological structures with the ratio of the Fourier amplitude  $A_2/A_0$  larger than 0.3, and with the  $m=2$  phase maintained nearly constant in the bar region (Table 2). For these bars the  $m=4$  amplitudes are also pronounced, there is a clear maximum in the  $Q_T$ -profile in the bar region and the “butterfly pattern” shows four regular structures. The  $Q_T$ -profiles and the “butterfly patterns” for these galaxies are shown in Fig. 7, showing also the  $m=0, 2$ , and 4 surface brightness profiles. The length of the region with a constant  $m=2$  phase was taken to be a measure of the bar length. Both the  $m=2$  and  $m=4$  phases are maintained nearly constant in the bar region, but in some cases the  $m=4$  amplitude drops at a slightly shorter distance, in which case we used the mean length of the constant  $m=2$  and  $m=4$  phases as the bar length.

In addition to the “classical bars”, other bar-like structures and non-axisymmetries are identified in many of the galaxies in our sample. Actually a large majority of galaxies have non-axisymmetric forces, manifested as maxima in the  $Q_T$ -profiles, whereas in 20 % no non-axisymmetric forces were detected above the background level ( $Q_b=0.01-0.1$ ). Due to differences in image quality no single minimum  $Q_b$ -value defines the bar-like potential. The non-axisymmetric forces presented in Table 3 deviate from the “classical bars” in a sense that the  $m=2$  phase is not maintained constant in the assumed bar region and the regular “butterfly patterns” do not necessarily appear in the force field. In 15 % of the galaxies in our sample the  $Q_T$  maxima are manifestations of strong spiral arms in the outer parts of the galactic disks.

As discussed by BB, both spherical and flattened bulges can affect  $Q_b$ -measurements: in a case of an intrinsically spherical bulge, the effect of assuming a bulge as thin as the disk is to overestimate the axisymmetric radial force and consequently to underestimate the relative bar strength. On the other hand, while de-projecting the image to face-on orientation bulges might cause artifacts in the direction of the minor-axis of the disk. The problem of large bulges was here avoided by limiting to those cases where the maximum tangential force appeared outside the bulge region. The small bulges still makes it difficult to detect mini-bars, but by subtracting the  $m=0$  component and by taking into account the de-projection effects, mini-bars could be detected for pgc 10488, 33371, 37999, 40153 and 43495, being previously identified also by Buta & Crocker (1993), Perez-Ramirez et al. (2000), Knapen et al. (1995), and by Block et al. (1994).

Based on the analytical work by Athanassoula (1992) the maximum ellipticity of a bar can be used as an approximation of bar strength, and its radial distance as an estimate of bar length. We calculated the ellipticity profiles using a method described in Laurikainen & Salo (2000) in which ellipses were iteratively fitted to the isophotes of the surface brightnesses. The maximum ellipticities  $\epsilon$  and their radial distances  $r_\epsilon$  in the bar region for the “classical bars” are shown in Table 2. In Laurikainen et al. (2002) these ellipticity measurements were utilized to show a good correlation between  $Q_b$  and  $\epsilon$ .

## 6 THE SAMPLE BIASES

The measurements reported in this work are used to compare bar strengths of the active and non-active galaxies (Laurikainen et al. 2002), so that it is important to study possible biases between different subgroups in the sample.

Active galaxies in our sample appeared to be somewhat brighter than the non-active systems, which is illustrated in Fig. 8a, showing also a weak correlation between the bar length and the absolute blue magnitude  $M_B$ , of the galaxy. However, while scaling the bar length to the scale-length of the disk, the bias was largely diluted (Fig. 8b). A similar correlation has been found previously by Kormendy (1979) for optically measured bar lengths. Due to the magnitude bias longer bars may have been selected for the active galaxies in our sample. However, we confirmed that this bias does not affect the mean bar strengths in the compared subsamples. This was checked by dividing the non-active galaxies to two magnitude bins with  $M_B$  larger and smaller than  $-19.8$  mag, resulting to practically identical mean forces,  $\langle Q_b \rangle = 0.22 \pm 0.10$  and  $0.24 \pm 0.12$ , respectively (the uncertainties indicate the sample standard deviations).



The relative number of barred galaxies rapidly drops in our sample when the inclination of the disk is larger than  $50^\circ$  (see Fig. 9). This is the case both for SAB and SB-galaxies and for the “classical bars” identified in the near-IR. The inclination distribution for the galaxies in the whole sample largely follows a random distribution of orientations,  $dN/di \sim \sin i$ , expected for an unbiased sample. Again, since in Laurikainen et al. we compare bar strengths between different subsamples it is important that this inclination bias does not affect the mean  $Q_b$ -values. It appeared that  $Q_b$  does not correlate with the inclination of the disk (see Fig. 10): especially for the galaxies with no “classical bars”  $Q_b$  is similar for all inclinations. For the galaxies with “classical bars” there may be a lack of strong bars among the nearly face-on galaxies ( $INC < 25^\circ$ ) and clearly among the highly inclined galaxies ( $INC > 60^\circ$ ), which is probably a manifestation of the uncertainties in the inclination determinations.

In order to check whether the dependence of bar detection frequency on inclination is specific for our sample or does appear also in larger samples of galaxies, we picked up all galaxies brighter than 15.5 mag from RC3 and constructed histograms for SA, SAB and SB-galaxies (Fig. 11), similar to those in Fig. 9. Evidently, a similar bias appears also in RC3: for SA-galaxies the inclinations are well sampled to  $60^\circ$ , for SB-galaxies to  $50^\circ$  and for SAB-galaxies the limit of well sampled galaxies is even lower than that. Quite surprisingly, the number of SAB-galaxies at inclinations larger than  $40^\circ$  drops much more rapidly than the number of SB-galaxies indicating that classification of a galaxy as SAB is very ambiguous. It also seems that in RC3 there is a deficiency of galaxies with very low assigned inclinations (less than  $20^\circ$ ), supporting the above interpretation that the lack of strong bars in nearly face-on galaxies is solely due to uncertainties in the orientation parameters. The found inclination bias might be of importance for example when bar frequencies are compared between low and high redshift galaxies. In order to study a possible redshift dependence of the bias, barred galaxy fractions in two inclination bins were compared at two magnitude intervals in RC3. The bias was found to become more significant toward the fainter galaxies: the relative number of SB galaxies with  $INC > 50^\circ$  dropped from 32 % to 25 % while going from the magnitude interval  $B_T < 12$  mag to  $B_T = 13.5 - 14.5$  mag, whereas the relative SB galaxy numbers with  $INC < 50^\circ$  were identical (38 %) in the two magnitude intervals. This means that when bar frequencies at high and low redshifts are compared, bar frequencies of distant galaxies are easily underestimated.

## 7 COMPARISON OF OPTICAL AND NEAR-IR BARS

The distributions of the non-axisymmetric forces among the de Vaucouleurs’s (1963) optical classes SA, SAB and SB are shown in Fig. 12 in J, H and K-bands. In agreement with BB and Block et al. (2001), the overlap between the different de Vaucouleurs’s types is significant. Based on estimating the ellipticities of bars, a somewhat different result was obtained by Abraham & Merrifield (2000), who argued that SB-galaxies are clearly separated from SA and SAB-galaxies in bar strength. In our sample SA and SAB galaxies have fairly similar non-axisymmetric forces, the only difference being that some SA galaxies have no non-axisymmetric forces.

Actually, it seems that SB-galaxies can belong to any of the bar strength classes from 1 to 6, as defined by BB. In our sample the minimum  $Q_b=0.09$  for SB galaxies is largely due to the image quality. We find that bars in SB galaxies are very similar to the “classical bars” in the near-IR: namely 95 % of all SB galaxies in our sample are classified as “classical” in the near-IR. They also have very similar bar strength distributions in Fig. 12. However, there are 30 % more “classical bars” than SB bars, the excess being distributed to all bar strengths, which means that even strong bars can be hidden by dust in the optical. In addition to bars significant tangential forces can be induced also by the spiral arms, especially in the outer parts of the disks, of which M51 (pgc 47404) is a good example. The spiral related forces may in some cases amount even to  $Q_b=0.26$ , corresponding to a bar strength class 3. This is quite interesting, because it means that even spiral arms can induce non-axisymmetric forces in the level typically associated with moderately strong bars. These non-axisymmetries may have important implications in secular evolution in galaxies, as for example for the onset of near nuclear star formation.

## 8 CONCLUSIONS

Non-axisymmetric forces are calculated for 107 spiral galaxies in J,H and K bands using a method where gravitational potentials are evaluated in a polar grid. Non-softened convolution function is applied and the vertical distribution of matter is approximated by an exponential function. The vertical scale-height of the disk is taken to be a certain fraction of the radial scale-length of the disk, and this ratio is assumed to be larger for the early than for the late-type galaxies. The M/L-ratio is assumed to be constant throughout the disk. The vertical mass distribution is generally assumed to obey the same formula everywhere in the galaxy, but tests were also performed to estimate the effect of radially non-constant vertical thickness. The phases of the Fourier density amplitudes are used to estimate the lengths of the bars. One of the main concerns of this study is to verify that the different methods of calculating the gravitational potential give mutually consistent results, most of the tests being carried out using a high quality H-image of NGC 1433 (Buta et al. 2001). In comparison to BB our method is more suitable for weak and noisy images. Also, it is possible to limit only to even Fourier decompositions, most likely to

characterize the non-axisymmetry related to the bar. Likewise in polar method it is easy to study distant-dependent  $h_z$ . The isophotal ellipticities of bars are also estimated, to facilitate comparisons to bar strengths estimated from maximal forces.

The main results are the following:

(1) Cartesian and polar grid methods for the potential evaluation are compared. In the Cartesian method the image is sampled to a density array and then 2D FFT in Cartesian coordinates is applied. In the polar grid method Fourier decomposition of density is calculated in a polar grid using FFT in azimuth and direct summation over radius. We found that similar results are obtained by these two methods for good quality images, provided that enough Fourier components (up to  $m=6$ ) are included, and the resolution of the Cartesian grid is sufficiently large.

(2) Bar strength is found to be rather insensitive to the vertical mass model of the disk, as long as a same vertical dispersion is assumed for all models (e.g.  $h_{sech2}/h_z = \sqrt{24}/\pi$ ,  $h_{sech}/h_z = \sqrt{8}/\pi$ ). Boxy/peanut shaped structures, in terms of non-constant vertical scale-heights along the disk, were also found to be quite unimportant for the evaluation of bar strengths. These parameters affect  $Q_b$  less than 5%. The largest uncertainties in  $Q_b$  are associated to the large scatter in the observed vertical scale-height of the disk within one Hubble type, and to the observed uncertainties in the orientation parameters of the disks, which both may induce uncertainties of about 10-15 % in  $Q_b$ .

(3) Significant non-axisymmetric forces ( $Q_b > 0.05$ ) are detected in 80 % of the galaxies in our sample. In most cases they were interpreted as bar-like features, based on significant  $m=2$  Fourier amplitudes in the bar regions and distinct “butterfly patterns” in the  $F_T / < F_R >$ -ratio maps. In 40% of the galaxies “classical bars” were detected, determined as having  $A_2/A_0 > 0.3$  and the  $m=2$  phases maintained nearly constant in the bar region. In some of the galaxies significant non-axisymmetric forces were detected in the outer parts of the disks connected to spiral arms, corresponding even to bar strength class 3.

(4) We confirm the previous result by BB and Block et al. (2001) showing the large overlap in bar strength between the optical SA, SAB and SB classes. Actually, SB-galaxy can belong to any of the bar strength classes between 1 and 6.

(5) We found that 95 % of SB galaxies in our sample belong to the “classical bars” identified in the near-IR, which means that the bars are similar. In the optical 1/3 of the “classical bars” are not classified as SB. Even bars which are in the optical obscured by dust and which become dust penetrated in the near-IR, cover all bar classes from 1 to 6, thus indicating that even strong bars can be obscured by dust.

(6) Bar lengths are estimated from the phases of the  $m=2$  and  $m=4$  Fourier components of density requiring that the phase is maintained nearly constant in the bar region. Bar length is found to correlate with the galaxy brightness  $M_B$ , confirming the previous result by Kormendy (1979) in the optical region.

(7) The number of SB-galaxies in our sample drops rapidly at inclinations  $> 50^\circ$ . A similar bias appears also in RC3 when limiting to galaxies brighter than 15.5 mag. This bias might have important implications while studying the frequencies of bars at low and high redshifts, especially because the bias increases toward fainter galaxies. Also, at high inclinations the number of SAB galaxies in RC3 drops much more rapidly than the number of SB-galaxies, thus being a manifestation of an ambiguous definition of the de Vaucouleurs’s SAB class.

## ACKNOWLEDGMENTS

We are grateful to Ron Buta for providing us with his H-band image of NGC 1433. This publication utilized images from the Two Micron All Sky Survey, which is a joint project of the University of Massachusetts and the Infrared Processing and Analysis Center/California Institute of Technology, funded by the National Aeronautics and Space Administration and the National Science Foundation. It also uses the NASA/IPAC Extra-galactic Database (NED), operated by the Jet Propulsion Laboratory in Caltech. We acknowledge the foundations of Magnus Ehrnrooth and the Academy of Finland of significant financial support.

## REFERENCES

- Abraham R.G., Merrifield M.R., 2000, AJ, 120, 2835
- Athanassoula E., 1992, MNRAS, 259, 328
- Athanassoula E., 2002, MNRAS, 330, 35
- Baggett W. E., Baggett S. M., Anderson K. S. J., 1998, AJ, 116, 1626
- Barnaby D., Thronson M. A., 1992, AJ, 103, 41
- Bell E. F., de Jong R. S., 2001, ApJ, 550, 212
- Block D., Puerari I. 1999, AA, 288, 365
- Block D.L., Wainscoat R.J. 1991, Nature, 353, 48
- Block D. L., Puerari I., Knapen J. H., Elmegreen B. G., Buta R., Stedman S., Elmegreen D. M., 2001, AA, 375, 761
- Block D. L., Bertin G., Stockton A., Grosbol P., Moorwood A. F. M., Peletier R. F., 1994, AA, 288, 365
- Burkhead A., Joshii Y., 1996, MNRAS, 282, 1349
- Buta R., 1986, ApJ, 61, 631
- Buta R., Block D. L. 2001, ApJ, 550, 243 (BB)

- Buta R., Crocker D. L., 1993, AJ, 105, 1344
- Buta R., Purcell G.B., Lewis M., Crocker D.A., Rautiainen P., Salo H., 1999, AJ, 117, 778
- Buta R., Ryder S., Madsen G., Wesson K., Crocker D.A., Combes F. 2001, AJ, 121, 225
- de Grijs R., Peletier R.F., van der Kruit P.C. 1997, AA, 327, 966
- de Grijs 1998, MNRAS, 299, 595
- de Vaucouleurs G. 1955, AJ, 60, 126
- 1963, ApJS, 8, 31
- de Vaucouleurs G. et al. 1991, Third Reference Catalogue of Bright Galaxies, New York, Springer, (RC3)
- Heraudeau Ph., Simien F., 1996, AAS, 118, 111
- de Jong R., van der Kruit P.C., 1994, ApJS, 106, 451
- de Jong R. S., 1996, AA, 313, 45
- Dove L. B., Thronson H. A., 1993, ApJ, 411, 632
- Elmegreen B.G., Elmegreen D.M., 1985, ApJ, 288, 438
- Elmegreen B., Elmegreen D., Montenegro L., 1989, ApJ, 343, 602
- Eskridge P. et al., 2000, AJ, 119, 536
- Ho L. C., Filippenko A. V., Sargent L. W., 1997, ApJ, 487, 591
- Hunt L.K., Malkan M.A., 1999, ApJ, 516, 660
- Knapen J. H., Schlosman I., Peletier R. F., 2000, ApJ, 529, 93
- Knapen J. H., Beckman J. E., Shlosman I., Peletier R. F., Heller C. H., de Jong R. S., 1995, ApJ, 443, L73
- Kormendy J., 1982, ApJ, 257, 75
- 1979, ApJ, 227, 714
- 1993, in Galactic Bulges, IAU Symp. No. 153, H. de Jonghe, H. J. Habing eds., Kluwer, Dordrecht, p. 209
- Kuijken K., 1991, ApJ, 372, 125
- Laurikainen E., Salo H., 2000, AAS, 141, 103
- Laurikainen E., Salo H., Rautiainen P., 2002, MNRAS, 331, 880
- Lutticke, R., Dettmar R.J., Pohlen M., 2000, AA, 362, 446
- Malkan M.A., Gorjian V., Tam R., 1998, ApJ, 117, 25
- Moles M., Marquez I., Perez E., 1995, ApJ, 438, 604
- Mulchaey J. S., Regan M. W., 1997, ApJ 482, L135
- Ohta K., 1996, in Barred Galaxies, R. Buta, D. A. Crocker, B. G. Elmegreen eds., ASP Conference Ser. Vol. 91, San Francisco, p. 37
- Perez-Ramirez D., Knapen J. H., Peletier R. F., Laine S., Doyon R., Nadeau D., 2000, MNRAS, 317, 234
- Quillen A. C., Frogel J. A., Gonzalez R. A., 1994, ApJ, 437, 162
- Roth J., 1994, AJ, 108, 862
- Schwarzkopf U., Dettmar R.J., 2001, AA, 373, 402
- Salo H., Rautiainen P., Buta R., Purcell C.B., Cobb M.L., Crocker D.A., Laurikainen E., 1999, AJ, 117, 792
- Sanchez-Portal M., Diaz A.I., Terlevich R., Terlevich E., 2000, MNRAS, 312, 2
- Seigar M.S., James P.A. 1998, MNRAS, 299, 672
- Sellwood J.A., Wilkinson A. 1993, Rep. Prog. Phys. 56, 173
- Smith J., Gehrz R.D., Grasdalen G.I., Hackwell J.A., Dietz R.D., Friedman S.D., 1990, ApJ, 362, 455
- Spillar et al., 1992, AJ, 103, 793
- Takamiya T., Sofue Y., 2000, ApJ, 534, 670
- Toth G., Ostriker J.P. 1992, ApJ, 389, 5
- Tully R. B., 1988, Nearby Galaxies Catalogue, Cambridge, Cambridge Univ. Press
- Tully R. B., 1974, ApJS, 27, 437
- van der Kruit P. C. & Searle L., 1981, AA, 95, 105
- van der Kruit P. C., 1988, AA, 95, 116
- Wainscoat R. J., Freeman K. C., Hyland A. R., 1989, ApJ, 337, 163
- Walker I.R., Mihos C., Herbig L., 1996, ApJ, 460, 121
- Yasuda N., Okamura S., Masataka F., 1995, ApJS, 96, 359

**FIGURE CAPTIONS**

**Figure 1.** Different models for the vertical density profile are compared. In the upper row the commonly used exponential,  $\text{sech}^2$  and  $\text{sech}$  laws are compared, with the scale-factor  $h$  chosen in a manner that yields identical slopes for  $z \gg h_z$ . The frame in the left displays the vertical profiles, while in the right the resulting convolution functions  $g$  are shown. These models correspond to those applied in Table 4 for calculation of  $Q_b$ . The lower row compares 5 different model profiles, including also Gaussian and uniform models. The scale-factors are chosen in a manner that yields the same vertical dispersion in each case. For comparison, the convolution function corresponding to 2D softened gravity is also shown, with softening parameter  $\epsilon = \sqrt{\langle z^2 \rangle}$ . These same models are applied for calculation of  $Q_T$ -profiles for NGC 1433 in Fig. 3.

**Figure 2.** Testing of the calculation method. The left hand frames show the results of our polar method applied to high quality H-band image of NGC 1433 (Buta et al. 2001), using different maximal numbers of even Fourier components as indicated in the frame. Fourier components were calculated with two pixel wide zones (1 pix = 1.141 arcsec), and the image was divided to 128 azimuthal bins. In the upper frame  $h_r/h_z = 2.5$ , typical for early-type galaxies, while the lower frame shows the influence of assuming 4 times thinner disk (For  $h_r = 45''$  and distance of 11.6 Mpc the studied  $h_z$  values are about 1 kpc and 0.25 kpc, respectively). For comparison, the right-hand frames show results using a Cartesian evaluation of the gravitational potential, with different number of grid divisions. The results for  $512 \times 512$  Cartesian grids are also super-posed on the left-hand curves.

**Figure 3.** The effect of using different vertical density laws on the obtained  $Q_T$ -profiles for NGC 1433. The density laws correspond to those in the lower row of Fig. 1 (scale-factors chosen to yield the same vertical dispersion), and the plot indicates how progressively more peaked vertical density profiles yield stronger non-axisymmetric forces. The two studied values of  $h_r/h_z$  are the same as in Fig. 2.: for thinner disk the precise form of the density profile is less significant.

**Figure 4.** The effect of radius-dependent scale-height on  $Q_T(r)$  profiles for NGC 1433. As in Fig 2, an exponential vertical profile is assumed for each distance, but with either positive ( $dh_z/dr = 0.05$ , solid curves) or negative ( $dh_z/dr = -0.05$ , dashed curves) gradient of the vertical scale height with distance. Three different cases are studied, where  $h_r/h_z = 2.5$ , either at  $r = 1, 2$ , or  $3h_r$ . The lines indicate the vertical scale height-profile in each case, with  $h_z$  multiplied by 0.01. According to Schwarzkopf & Dettmar (2001), the disk thickness often increases with radius, and  $dh_z/dr = 0.05$  corresponds to the maximum value observed for early types. Negative gradients are also studied, to emphasize the smallness of the expected maximal effect of vertically dependent  $h_z$ . For comparison, the crosses indicate the peak of the  $Q_T$  profile in the case of constant  $h_r/h_z = 2.5$ . The polar method is used.

**Figure 5.** A more detailed comparison of the effects of distance-dependent  $h_z$ , corresponding to the middle frame in Fig. 4, except that twice larger positive and negative gradients are studied, together with the case of constant  $h_z$ . The mean radial force profile is shown, together with the  $m = 2$  and  $m = 4$  Fourier amplitudes of the tangential force components (forces are in arbitrary units). As expected, tangential force components are increased in regions where scale height is reduced. The same is true also for the radial force, which however is even more strongly affected in the region of maximal  $F_T/F_R$  ratio, explaining the slightly reduced  $Q_T$  in the case of positive  $dh_z/dr$  gradient.

**Figure 6.** Bar strength measurements by BB and by us are compared for 13 galaxies in H-band. In both measurements the same orientation parameters were used and the vertical mass distribution was approximated by an exponential profile with  $h_z = 325 \text{ kpc}$  ( $H_0 = 75 \text{ km s}^{-1} \text{ Mpc}^{-1}$ ). The  $m = 0, 2, 4, 6$  Fourier components of density were included, and calculated for radial annulae with width of  $2''$ . In the azimuthal direction 128 divisions were used in all cases. No softening was used in our potential evaluation.

**Figure 7.** For the “classical barred” galaxies in the near-IR we show: the original 2MASS image in the plane of the sky ( $1^{\text{th}}$  column), the same image de-projected to face-on orientation, with the  $m=0$  Fourier component being subtracted ( $2^{\text{th}}$  column), the “butterfly pattern” ( $3^{\text{th}}$  column), the  $m=0,2,4$  surface density profiles ( $4^{\text{th}}$  column) and the radial  $Q_T$ -profile ( $5^{\text{th}}$  column). The “butterfly patterns” were calculated from the potentials using all even and odd components up to  $m=6$ , while in the  $Q_T$ -profiles all even components up to 10 were included. In the butterfly diagrams the thick contours correspond to  $Q_T$  levels of 0.1, 0.2, 0.3, 0.4, 0.5, while the thin contours refer to corresponding negative levels. In the  $Q_T$ -profiles the thin lines show measurements in the four image quadrants, whereas the thick lines show the mean values. The dashed vertical line in the  $Q_T$ -profile shows the length of the bar estimated from the phases of  $m=2$  and  $m=4$  density components as explained in the text. The numbers in the upper right corner give the values for the maximum  $Q_T$  in the bar region and its radial distance. The maximum is also shown by the box symbol in the  $Q_T$ -profiles. In the de-projected image the solid circle indicates the location of the maximum  $Q_T$  and the dashed circle the measurement region.

**Figure 8.** Absolute blue magnitude v.s. bar length. The magnitudes are from RC3 and bar lengths are estimated from the phases of the  $m=2$  Fourier amplitudes as explained in the text. In Fig. 8a bar lengths are given in absolute units, using the distances from Tully (1988), and in Fig. 8b they are scaled to the scale-length of the disk.  $H = 75 \text{ km s}^{-1} \text{ Mpc}^{-1}$ .

**Figure 9.** The inclination distribution of the galaxies in our sample, SB galaxies and the “classical bars” identified in the near-IR (see the text) being shown separately. For comparison, the inclination distribution for all galaxies in our sample is also shown. The dashed line indicates a random distribution of inclinations, normalized to the maximum inclination and

the number of galaxies in the sample.

**Figure 10.** A correlation between the inclination of the disk (INC) and bar strength ( $Q_b$ ) for the galaxies in our sample.

**Figure 11.** A similar figure as Fig. 9, but shown for the de Vaucouleurs’s (1963) classes SA, SAB and SB for a magnitude-limited sample ( $B_T < 15.5\ mag$ ) from RC3.

**Figure 12.** Distribution of the non-axisymmetric forces among the de Vaucouleurs’s (1963) classes SA, SAB and SB, measured in J, H and K-bands (Figs a, b and c, respectively). For comparison, bar strength distribution is shown also for the “classical bars” identified in the near-IR. Notice that not all non-axisymmetric forces in the figure are associated to bar-like potentials, being due to spiral arms for some SA and SAB-galaxies.

**Table 1.** General properties of the galaxies in the sample.

| pgc   | ngc   | $T_m$   | $B_T$ | PA      | INC     | Dist.[Mpc] | $h_R[']$    | act     |
|-------|-------|---------|-------|---------|---------|------------|-------------|---------|
| 2081  | N157  | .SXT4.. | 11.00 | 40      | 49.8    | 20.9       | 35.8(V)(6)  |         |
| 2437  | N210  | .SXS3.. | 11.60 | 160     | 48.6    | 20.3       | 15*         |         |
| 3051  | N278  | .SXT3.. | 11.47 | -       | 17.3    | 11.8       | 13*         |         |
| 3089  | N289  | .SBT4.. | 11.72 | 130     | 44.9    | 19.4       | 14.0(V)(6)  |         |
| 5619  | N578  | .SXT5.. | 11.44 | 110     | 50.9    | 19.5       | 38*         |         |
| 5818  | N598  | .SAS6.. | 6.27  | 23      | 53.9    | 0.7        | 533.3(V)(6) | HII     |
| 7525  | N772  | .SAS3.. | 11.09 | 125(1)  | 50.2(1) | 32.3       | 56*         |         |
| 9057  | N908  | .SAS5.. | 10.83 | 75      | 64.1    | 17.8       | 45*         |         |
| 10122 | N1042 | .SXT6.. | 11.56 | 155**   | 12.2    | 16.7       | 57.9(V)(6)  |         |
| 10266 | N1068 | RSAT3.. | 9.61  | 70      | 31.7    | 14.4       | 21.4*       | Sy1/Sy2 |
| 10464 | N1084 | .SAS5.. | 11.31 | 25**    | 55.8    | 17.1       | 19*         |         |
| 10488 | N1097 | .SBS3.. | 10.23 | 130     | 47.5    | 14.5       | 39*         | Sy1     |
| 10496 | N1087 | .SXT5.. | 11.46 | 5       | 52.9    | 19.0       | 20.1(V)(6)  |         |
| 11479 | N1187 | .SBR5.. | 11.34 | 130     | 42.2    | 16.3       | 23.3(V)(6)  |         |
| 11819 | N1232 | .SXT5.. | 10.52 | 108     | 29.4    | 21.1       | 42*         |         |
| 12007 | N1255 | .SXT4.. | 11.40 | 117     | 50.9    | 19.9       | 29.8(V)(6)  |         |
| 12412 | N1300 | .SBT4.. | 11.11 | 106     | 48.6    | 18.8       | 76.6(V)(6)  |         |
| 12431 | N1302 | RSBR0.. | 11.60 | -       | 17.3    | 20.0       | 65*         |         |
| 12626 | N1309 | .SAS4*. | 11.97 | 45      | 21.0    | 26.0       | 14*         |         |
| 13059 | N1350 | PSBR2.. | 11.16 | 0       | 57.5    | 16.9       | 31*         | Sy      |
| 13255 | N1367 | .SXT1.. | 11.57 | 135     | 46.2    | 17.1       | 50.6(V)(6)  |         |
| 13368 | N1385 | .SBS6.. | 11.45 | 165     | 55.0(5) | 17.5       | 29.2(V)(6)  |         |
| 13434 | N1398 | PSBR2.. | 10.57 | 100     | 40.7    | 16.1       | 29.4(V)(6)  | Sy      |
| 13602 | N1425 | PSBR2.. | 11.29 | 129     | 63.5    | 17.4       | 46.5(V)(6)  | Sy      |
| 14814 | N1559 | .SBS6.. | 11.00 | 64      | 60.0    | 14.3       | 31*         |         |
| 15821 | N1637 | .SXT5.. | 11.47 | 15      | 35.6    | 8.9        | 38.0*       |         |
| 16709 | N1792 | .SAT4.. | 10.87 | 137     | 59.9    | 13.6       | 34*         |         |
| 16779 | N1808 | RSXS1.. | 10.74 | 133     | 53      | 10.8       | 26.9(I)(4)  | Sy2     |
| 16906 | N1832 | .SBR4.. | 11.96 | 10      | 48.6    | 23.5       | 15.3(V)(6)  |         |
| 18258 | N2139 | .SXT6.. | 11.99 | 0**     | 0**     | 22.4       | 19.7(V)(6)  |         |
| 18602 | N2196 | PSAS1.. | 11.82 | 35      | 39.1    | 28.8       | 27.2(V)(6)  |         |
| 19531 | N2280 | .SAS6.. | 10.90 | 163     | 60.7    | 23.2       | 45.1(V)(6)  |         |
| 25069 | N2655 | .SXS0.. | 10.96 | -       | 33.7    | 24.4       | 52*         | Sy2     |
| 26259 | N2835 | .SBT5.. | 11.01 | 8       | 48.6    | 10.8       | 62.6(V)(6)  |         |
| 26512 | N2841 | .SAR3*. | 10.09 | 147     | 64.1    | 12.0       | 45.0(V)(6)  | Sy1/L   |
| 27077 | N2903 | .SXT4.. | 9.68  | 17      | 60.0(4) | 6.3        | 54.5(V)(6)  | HII     |
| 27777 | N2964 | .SXR4*. | 11.99 | 97      | 56.7    | 25.9       | 21.2(V)(6)  | HII     |
| 28120 | N2976 | .SA.5P. | 10.82 | 141(1)  | 55.2(1) | 2.1        | 45*         | HII     |
| 28316 | N2985 | PSAT2.. | 11.18 | 2(1)    | 36.9(1) | 22.4       | 35*         | L       |
| 28630 | N3031 | .SAS2.. | 7.89  | 157     | 58.3    | 1.4        | 157.5(V)(6) | Sy1.8/L |
| 29146 | N3077 | .I.O.P. | 10.61 | 45      | 33.7    | 2.1        | 44*         | HII     |
| 30087 | N3184 | .SXT6.. | 10.36 | 135     | 21.1    | 8.7        | 74.0(V)(6)  | HII     |
| 30445 | N3227 | .I.O.P. | 11.10 | 155     | 47.5    | 23.4       | 23.6(V)(6)  | HII     |
| 31650 | N3310 | .SXR4P. | 11.15 | -       | 39.1    | 18.7       | 123.0(V)(6) | HII     |
| 31883 | N3338 | .SAS5.. | 11.64 | 100     | 51.9    | 22.8       | 25.3(V)(6)  |         |
| 32183 | N3359 | .SBT5.. | 11.03 | 170     | 52.9    | 19.2       | 36*         | HII     |
| 33166 | N3486 | .SXR5.. | 11.05 | 111(1)  | 24.5(1) | 7.4        | 36*         | Sy2     |
| 33371 | N3504 | RSXS2.. | 11.82 | -       | 39.1    | 26.5       | 21.9(V)(6)  | HII     |
| 33390 | N3507 | .SBS3.. | 11.73 | 90(2)   | 21.6(2) | 19.8       | 25.0(K)(5)  | L       |
| 33550 | N3521 | .SXT4.. | 9.83  | 163     | 57.0(5) | 7.2        | 37.7(I)(4)  | L       |
| 34298 | N3596 | .SXT5.. | 11.95 | 139(2)  | 28.4(2) | 23.0       | 27.9(B)(5)  |         |
| 35164 | N3675 | .SAS3.. | 11.00 | 2(1)    | 57.3(1) | 12.8       | 34*         |         |
| 35193 | N3681 | .SXR4.. | 11.90 | 103(2)  | 32.9(2) | 24.2       | 14.0(K)(5)  |         |
| 35268 | N3686 | .SBS4.. | 11.89 | 13.1(2) | 41.4(2) | 23.5       | 27.6(B)(5)  |         |
| 35616 | N3718 | .SBS1P. | 11.59 | 173(1)  | 52.0(1) | 17.0       | 41.4(V)(6)  | Sy1     |
| 35676 | N3726 | .SXR5.. | 10.91 | 10.0    | 46.4    | 17.0       | -           |         |

Table 1. continued

| pgc   | ngc   | $T_m$   | $B_T$ | PA      | INC      | Dist.[Mpc] | $h_R$ [ <sup>4</sup> ] | act       |
|-------|-------|---------|-------|---------|----------|------------|------------------------|-----------|
| 36921 | N3898 | .SAS2.. | 11.60 | 107     | 53.9     | 21.9       | 37.8(V)(6)             | HII/L     |
| 37773 | N4027 | .SBS8.. | 11.66 | 167     | 40.7     | 25.6       | 25.3(V)(6)             |           |
| 37999 | N4041 | .SAT4*. | 11.88 | -       | 21.1     | 22.7       | 17*                    |           |
| 38150 | N4062 | .SAS5.. | 11.90 | 100(1)  | 65.8(1)  | 9.7        | 24.7(V)(6)             | HII       |
| 38739 | N4151 | PSXT2*. | 11.50 | 50(7)   | 16.3(9)  | 15.5       | 36*                    | Sy1.5     |
| 39578 | N4254 | .SAS5.. | 10.44 | 40**    | 29.4     | 16.8       | 34.8(V)(6)             |           |
| 39724 | N4274 | RSBR2.. | 11.34 | 102(1)  | 67.0(1)  | 9.7        | 56.9(V)(6)             |           |
| 39907 | N4293 | RSBS0.. | 11.26 | 72      | 65.0(3)  | 17.0       | 42.9(V)(6)             | L         |
| 40097 | N4314 | .SBT1.. | 11.43 | -       | 27.0     | 9.7        | 43.3*                  | L         |
| 40153 | N4321 | .SXS4.. | 10.05 | 153(2)  | 27.1(2)  | 16.8       | 64.0(B)(5)             | HII/L     |
| 40614 | N4394 | RSBR3.. | 11.73 | -       | 25.0(3)  | 16.8       | 33.0(V)(6)             | L         |
| 40692 | N4414 | .SAT5.. | 10.96 | 161(1)  | 45.6(1)  | 9.7        | 27.6(V)(6)             |           |
| 41024 | N4450 | .SAS2.. | 10.90 | 171(2)  | 46.4(2)  | 16.8       | 44.8(K)(5)             | L         |
| 41333 | N4490 | .SBS7P. | 10.22 | 125     | 60.7     | 9.3        | 38.4(V)(6)             |           |
| 41517 | N4501 | .SAT3.. | 10.36 | 140     | 57.5     | 16.8       | 47.0(V)(6)             | Sy2       |
| 41934 | N4548 | .SBT3.. | 10.96 | 150     | 37.4     | 16.8       | 28.7(V)(6)             | Sy/L      |
| 42089 | N4569 | .SXT2.. | 10.26 | 23      | 62.8     | 16.8       | 73.5(V)(6)             | Sy/L      |
| 42575 | N4618 | .SBT9.. | 11.22 | 25      | 35.6     | 8.2        | 60*                    | HII       |
| 42833 | N4651 | .SAT5.. | 11.39 | 73.9(2) | 47.9(2)  | 16.8       | 25.1(B)(5)             | L         |
| 42857 | N4654 | .SXT6.. | 11.10 | 128     | 57.0(3)  | 16.8       | 39.8(V)(6)             |           |
| 43186 | N4689 | .SAT4.. | 11.60 | 155**   | 40.0(3)  | 16.8       | 38.9(V)(6)             |           |
| 43238 | N4691 | RSBS0P. | 11.66 | 15      | 35.6(4)  | 22.5       | 35.8(V)(6)             |           |
| 43321 | N4699 | .SXT3.. | 10.41 | 45      | 46.2     | 25.7       | -                      | Sy        |
| 43495 | N4736 | RSAR2.. | 8.99  | 105     | 35.6     | 4.3        | 84.3(V)(6)             | L         |
| 43507 | N4731 | .SBS6.. | 11.90 | 85      | 60.7     | 25.9       | 39*                    |           |
| 43671 | N4753 | .I.0... | 10.85 | 80      | 62.1     | 15.1       | 46*                    |           |
| 44182 | N4826 | RSAT2.. | 9.36  | 115     | 57.      | 4.1        | 61.9(V)(6)             | Sy2       |
| 45165 | N4941 | RSXR2*. | 12.43 | 15      | 57.5     | 6.4        | 21.6(V)(6)             | Sy2       |
| 45749 | N5005 | .SXT4.. | 10.61 | 67(1)   | 65.0**   | 21.3       | 33.0(V)(6)             | Sy2       |
| 45948 | N5033 | .SAS5.. | 10.75 | 173(1)  | 60.0(1)  | 18.7       | 731.6(V)(6)            | Sy1.9     |
| 46247 | N5054 | .SAS4.. | 11.67 | 155     | 54.0(4)  | 27.3       | 40.3(I)(4)             |           |
| 46400 | N5068 | .SXT6.. | 10.52 | 110     | 29.4     | 6.7        | 39.3(V)(6)             |           |
| 47404 | N5194 | .SAS4P. | 8.96  | 170(8)  | 20.0(8)  | 9.3        | 107.5(V)(6)            | HII/Sy2.5 |
| 47413 | N5195 | .I.0.P. | 10.45 | 90(9)   | 30.0(9)  | 7.7        | 29*                    | L         |
| 48171 | N5247 | .SAS4.. | 10.50 | 20      | 29.4     | 22.2       | 62*                    |           |
| 50063 | N5457 | .SXT6.. | 8.31  | -       | 21.1     | 5.4        | 143.4(V)(6)            |           |
| 52412 | N5713 | .SXT4P. | 12.18 | 10      | 27.0     | 30.4       | 13.8(V)(6)             |           |
| 55588 | N5962 | .SAR5.. | 11.98 | 96.1(2) | 44.8 (2) | 31.8       | 17.9(B)(5)             | HII       |
| 56219 | N6015 | .SAS6.. | 11.69 | 28(1)   | 61.3(1)  | 17.5       | 37.1(V)(6)             | HII       |
| 58477 | N6217 | RSBT4.. | 11.79 | 150**   | 33.7     | 23.9       | 13.2(V)(6)             | Sy2       |
| 61742 | N6643 | .SAT5.. | 11.73 | 40(1)   | 60.0(1)  | 25.5       | 27.7(V)(6)             |           |
| 68096 | N7217 | RSAR2.. | 11.02 | 95      | 33.7     | 16.0       | 26.9(V)(6)             | Sy        |
| 68165 | N7213 | .SAS1*. | 11.01 | -       | 26.9     | 22.0       | 82*                    | Sy1.5     |
| 69253 | N7314 | .SXT4.. | 11.88 | 3       | 62.8     | 18.3       | -                      | Sy1.9     |
| 69327 | N7331 | .SAS3.. | 10.35 | 170(1)  | 62.6(1)  | 14.3       | 89.4(V)(6)             | L         |
| 70419 | N7479 | .SBS5.. | 11.60 | 40.5(2) | 39.6(2)  | 32.4       | 50.7(B)(5)             | Sy2/L     |
| 70714 | N7513 | PSBS3P. | 11.39 | 108     | 48.6     | 21.3       | 55*                    |           |
| 71047 | N7606 | .SAS3.. | 11.51 | 146(1)  | 67.7(1)  | 28.9       | 43*                    |           |
| 72009 | N7723 | .SBR3.. | 11.94 | 35      | 47.5     | 23.7       | 19*                    |           |
| 72060 | N7727 | .SXS1P. | 11.50 | 35      | 40.7     | 23.3       | -                      |           |
| 72237 | N7741 | .SBS6.. | 11.84 | 170(2)  | 45.6(2)  | 12.3       | 52.7(B)(5)             |           |

(1) Heraudeau &amp; Simien (1996).

(2) de Jong &amp; van der Kruit (1994).

(3) Yasuda et al. (1995).

(4) Roth (1994).

(5) de Jong 1996.

(6) Bagget et al. 1998.

(7) Sanchez-Portal et al. (2000).

(8) Tully (1974).

(9) Smith et al. (1990).

\* estimated from 2MASS images.

\*\* own estimate from the Digitized Sky Survey plate.

**Table 2.**  $Q_b$ ,  $r_{Qb}$ ,  $\epsilon$  and  $r_\epsilon$  for galaxies with classical bars in the near-IR.

| pgc   | $Q_H$           | $r_H ["]$ | $Q_J$           | $r_J ["]$ | $Q_K$           | $r_K ["]$ | length ["] | $\epsilon$ | $r_\epsilon ["]$ |
|-------|-----------------|-----------|-----------------|-----------|-----------------|-----------|------------|------------|------------------|
| 3089  | $0.15 \pm 0.00$ | 13        | $0.14 \pm 0.00$ | 15        | $0.17 \pm 0.03$ | 15        | 20         | 0.39       | 20.28            |
| 10266 | $0.15 \pm 0.01$ | 11        | $0.16 \pm 0.02$ | 11        | $0.12 \pm 0.01$ | 11        | 25         | 0.43       | 14.96            |
| 10488 | $0.24 \pm 0.01$ | 79        | $0.24 \pm 0.02$ | 79        | $0.23 \pm 0.01$ | 77        | 120        | 0.58       | 94.72            |
| 10496 | $0.42 \pm 0.00$ | 11        | $0.43 \pm 0.01$ | 11        | $0.44 \pm 0.01$ | 11        | 22         | 0.63       | 24.26            |
| 11479 | $0.19 \pm 0.03$ | 29        | $0.19 \pm 0.02$ | 31        | $0.21 \pm 0.03$ | 27        | 40         | 0.55       | 41.42            |
| 12412 | $0.40 \pm 0.03$ | 61        | $0.38 \pm 0.01$ | 59        | $0.41 \pm 0.04$ | 59        | 80         | 0.71       | 68.77            |
| 12431 | $0.09 \pm 0.02$ | 19        | $0.09 \pm 0.01$ | 19        | $0.09 \pm 0.04$ | 19        | 30         | 0.35       | 28.06            |
| 13059 | $0.29 \pm 0.01$ | 69        | $0.30 \pm 0.00$ | 71        | $0.30 \pm 0.00$ | 69        | 110        | 0.62       | 77.30            |
| 13368 | $0.37 \pm 0.01$ | 35        | $0.35 \pm 0.02$ | 35        | $0.35 \pm 0.02$ | 11        | 45         | 0.70       | 9.91             |
| 13434 | $0.20 \pm 0.00$ | 39        | $0.21 \pm 0.01$ | 39        | $0.20 \pm 0.00$ | 39        | 60         | 0.54       | 49.76            |
| 13602 | $0.16 \pm 0.00$ | 11        | $0.15 \pm 0.01$ | 11        | $0.15 \pm 0.01$ | 11        | 25         | 0.48       | 4.73             |
| 14814 | $0.30 \pm 0.02$ | 11        | $0.27 \pm 0.02$ | 13        | $0.24 \pm 0.00$ | 13        | 15         | 0.51       | 13.58            |
| 15821 | $0.20 \pm 0.05$ | 19        | $0.23 \pm 0.00$ | 18        | $0.24 \pm 0.04$ | 17        | 25         | 0.56       | 24.74            |
| 16906 | $0.23 \pm 0.01$ | 13        | $0.23 \pm 0.00$ | 15        | $0.22 \pm 0.01$ | 13        | 20         | 0.49       | 18.46            |
| 18258 | $0.35 \pm 0.01$ | 7         | $0.33 \pm 0.01$ | 5         | $0.35 \pm 0.07$ | 7         | 25         | 0.56       | 0.00             |
| 26259 | $0.28 \pm 0.01$ | 15        | $0.31 \pm 0.00$ | 11        | $0.38 \pm 0.01$ | 15        | 30         | 0.58       | 33.18            |
| 27077 | $0.26 \pm 0.05$ | 61        | $0.25 \pm 0.01$ | 63        | $0.27 \pm 0.00$ | 61        | 75         | 0.65       | 65.81            |
| 27777 | $0.32 \pm 0.00$ | 21        | $0.33 \pm 0.01$ | 21        | $0.33 \pm 0.01$ | 23        | 30         | 0.63       | 26.31            |
| 32183 | $0.46 \pm 0.05$ | 11        | $0.42 \pm 0.01$ | 11        | $0.45 \pm 0.03$ | 11        | 55         | 0.65       | 9.46             |
| 33371 | $0.26 \pm 0.02$ | 27        | $0.27 \pm 0.03$ | 29        | $0.26 \pm 0.02$ | 29        | 45         | 0.63       | 30.91            |
| 33390 | $0.19 \pm 0.04$ | 17        | $0.21 \pm 0.00$ | 21        | $0.20 \pm 0.06$ | 21        | 20         | 0.44       | 20.99            |
| 35268 | $0.33 \pm 0.01$ | 11        | $0.28 \pm 0.02$ | 13        | $0.30 \pm 0.01$ | 11        | 29         | 0.59       | 22.25            |
| 35616 | $0.12 \pm 0.01$ | 65        | $0.16 \pm 0.02$ | 60        | $0.14 \pm 0.01$ | 60        | 80         | 0.38       | 50.00            |
| 37773 | $0.50 \pm 0.01$ | 11        | $0.51 \pm 0.02$ | 11        | $0.48 \pm 0.02$ | 11        | 20         | 0.67       | 7.58             |
| 37999 | $0.13 \pm 0.02$ | 11        | $0.08 \pm 0.00$ | 11        | $0.09 \pm 0.01$ | 11        | 20         | 0.33       | 6.07             |
| 38739 | $0.16 \pm 0.02$ | 67        | $0.18 \pm 0.03$ | 67        | $0.14 \pm 0.01$ | 67        | 100        | 0.52       | 75.72            |
| 39724 | $0.31 \pm 0.03$ | 45        | $0.31 \pm 0.00$ | 41        | $0.31 \pm 0.02$ | 45        | 100        | 0.65       | 66.93            |
| 39907 | $0.22 \pm 0.06$ | 47        | $0.22 \pm 0.01$ | 49        | $0.21 \pm 0.02$ | 47        | 90         | 0.50       | 60.00            |
| 40097 | $0.33 \pm 0.01$ | 47        | $0.33 \pm 0.00$ | 45        | $0.34 \pm 0.00$ | 45        | 88         | 0.68       | 67.71            |
| 40614 | $0.22 \pm 0.01$ | 29        | $0.21 \pm 0.00$ | 27        | $0.22 \pm 0.01$ | 25        | 65         | 0.61       | 43.26            |
| 41024 | $0.13 \pm 0.01$ | 39        | $0.13 \pm 0.01$ | 39        | $0.17 \pm 0.01$ | 41        | 60         | 0.41       | 46.65            |
| 41934 | $0.33 \pm 0.02$ | 49        | $0.32 \pm 0.01$ | 47        | $0.32 \pm 0.00$ | 45        | 70         | 0.62       | 76.98            |
| 42575 | $0.40 \pm 0.03$ | 10        | $0.36 \pm 0.03$ | 11        | $0.36 \pm 0.01$ | 13        | 45         | 0.65       | 16.72            |
| 43238 | $0.61 \pm 0.01$ | 11        | $0.59 \pm 0.01$ | 13        | $0.63 \pm 0.00$ | 11        | 60         | 0.77       | 17.97            |
| 43507 | $1.19 \pm 0.10$ | 23        | $1.07 \pm 0.00$ | 25        | $1.27 \pm 0.02$ | 25        | 100        | 0.86       | 0.00             |
| 46400 | $0.43 \pm 0.03$ | 11        | $0.41 \pm 0.01$ | 13        | $0.48 \pm 0.04$ | 13        | 52         | 0.65       | 20.00            |
| 47413 | $0.14 \pm 0.01$ | 39        | $0.15 \pm 0.00$ | 39        | $0.13 \pm 0.01$ | 41        | 48         | 0.46       | 51.49            |
| 52412 | $0.37 \pm 0.04$ | 11        | $0.39 \pm 0.05$ | 13        | $0.39 \pm 0.02$ | 13        | 28         | 0.57       | 20.21            |
| 58477 | $0.36 \pm 0.01$ | 29        | $0.40 \pm 0.01$ | 25        | $0.40 \pm 0.04$ | 29        | 40         | 0.69       | 35.98            |
| 70419 | $0.63 \pm 0.03$ | 37        | $0.62 \pm 0.02$ | 39        | $0.65 \pm 0.04$ | 43        | 70         | 0.78       | 49.71            |
| 70714 | $0.46 \pm 0.02$ | 17        | $0.41 \pm 0.01$ | 25        | $0.46 \pm 0.01$ | 20        | 55         | 0.76       | 37.84            |
| 72009 | $0.30 \pm 0.02$ | 16        | $0.28 \pm 0.03$ | 15        | $0.31 \pm 0.01$ | 17        | 28         | 0.64       | 20.20            |
| 72237 | $0.64 \pm 0.02$ | 11        | $0.70 \pm 0.02$ | 16        | $0.70 \pm 0.05$ | 13        | 70         | 0.77       | 0.00             |



**Table 3.** Bar strengths for galaxies without classical bars.

| pgc   | $Q_H$           | $r_H[']$ | $Q_J$           | $r_J[']$ | $Q_K$           | $r_K[']$ | comment |
|-------|-----------------|----------|-----------------|----------|-----------------|----------|---------|
| 2081  | $0.29 \pm 0.11$ | 33       | $0.26 \pm 0.00$ | 31       | $0.26 \pm 0.01$ | 35       | S       |
| 2437  | $0.12 \pm 0.00$ | 33       | $0.12 \pm 0.01$ | 33       | $0.11 \pm 0.00$ | 33       | BM      |
| 3051  | $0.06 \pm 0.02$ | 23       | $0.06 \pm 0.01$ | 25       | $0.06 \pm 0.01$ | 23       |         |
| 5619  | $0.32 \pm 0.01$ | 11       | $0.28 \pm 0.01$ | 11       | $0.33 \pm 0.08$ | 11       | BM      |
| 5818  | $0.24 \pm 0.00$ | 49       | $0.25 \pm 0.04$ | 35       | $0.29 \pm 0.00$ | 35       | BM      |
| 7525  | $0.10 \pm 0.02$ | 33       | $0.10 \pm 0.02$ | 35       | $0.12 \pm 0.00$ | 35       |         |
| 9057  | $0.18 \pm 0.02$ | 71       | $0.19 \pm 0.00$ | 67       | $0.17 \pm 0.02$ | 61       | S       |
| 10122 | $0.38 \pm 0.00$ | 25       | $0.35 \pm 0.06$ | 23       | $0.38 \pm 0.02$ | 25       | BM      |
| 10464 | $0.18 \pm 0.02$ | 29       | $0.18 \pm 0.01$ | 33       | $0.19 \pm 0.03$ | 33       | B       |
| 11819 | $0.17 \pm 0.01$ | 11       | $0.16 \pm 0.01$ | 11       | $0.20 \pm 0.03$ | 11       | BM      |
| 12007 | $0.15 \pm 0.02$ | 25       | $0.15 \pm 0.02$ | 20       | $0.18 \pm 0.03$ | 25       | S       |
| 12626 | $0.15 \pm 0.06$ | 15       | $0.12 \pm 0.02$ | 15       | $0.14 \pm 0.02$ | 15       | B       |
| 13255 | $0.12 \pm 0.02$ | 21       | $0.12 \pm 0.00$ | 21       | $0.15 \pm 0.00$ | 23       | BM      |
| 16709 | $0.25 \pm 0.00$ | 33       | $0.24 \pm 0.00$ | 33       | $0.26 \pm 0.00$ | 33       | S       |
| 16779 | $0.25 \pm 0.00$ | 69       | $0.27 \pm 0.00$ | 67       | $0.23 \pm 0.00$ | 71       | BM      |
| 18602 | $0.07 \pm 0.00$ |          | $0.09 \pm 0.02$ |          | $0.10 \pm 0.04$ |          |         |
| 19531 | $0.17 \pm 0.02$ | 45       | $0.17 \pm 0.02$ | 45       | $0.17 \pm 0.03$ | 45       | BM      |
| 25069 | $0.12 \pm 0.01$ |          | $0.13 \pm 0.01$ |          | $0.13 \pm 0.03$ |          | B       |
| 26512 | $0.18 \pm 0.01$ | 13       | $0.19 \pm 0.01$ | 13       | $0.19 \pm 0.01$ | 13       | BM      |
| 28120 | $0.30 \pm 0.01$ | 57       | $0.30 \pm 0.02$ | 61       | $0.35 \pm 0.01$ | 63       | BM      |
| 28316 | $0.03 \pm 0.03$ |          | $0.02 \pm 0.01$ |          | $0.02 \pm 0.02$ |          |         |
| 28630 | $0.06 \pm 0.02$ |          | $0.06 \pm 0.02$ |          | $0.06 \pm 0.02$ |          |         |
| 29146 | $0.07 \pm 0.03$ |          | $0.09 \pm 0.01$ |          | $0.07 \pm 0.03$ |          |         |
| 30087 | $0.16 \pm 0.01$ | 45       | $0.15 \pm 0.01$ | 45       | $0.15 \pm 0.01$ | 45       | S       |
| 30445 | $0.18 \pm 0.07$ | 49       | $0.18 \pm 0.01$ | 41       | $0.19 \pm 0.00$ | 53       | B       |
| 31650 | $0.06 \pm 0.01$ |          | $0.04 \pm 0.00$ |          | $0.07 \pm 0.00$ |          |         |
| 31883 | $0.12 \pm 0.01$ | 45       | $0.14 \pm 0.05$ | 49       | $0.16 \pm 0.03$ | 45       | S       |
| 33166 | $0.16 \pm 0.00$ | 17       | $0.15 \pm 0.00$ | 60       | $0.16 \pm 0.00$ | 60       | BM      |
| 33550 | $0.02 \pm 0.00$ |          | $0.06 \pm 0.01$ |          | $0.06 \pm 0.01$ |          |         |
| 34298 | $0.16 \pm 0.01$ | 23       | $0.16 \pm 0.04$ | 19       | $0.16 \pm 0.02$ | 34       | S       |
| 35164 | $0.04 \pm 0.01$ |          | $0.04 \pm 0.00$ |          | $0.04 \pm 0.03$ |          | S       |
| 35193 | $0.25 \pm 0.01$ | 8        | $0.21 \pm 0.02$ | 9        | $0.23 \pm 0.01$ | 8        | BM      |
| 35676 | $0.33 \pm 0.04$ | 23       | $0.30 \pm 0.01$ | 27       | $0.30 \pm 0.05$ | 29       | BM      |
| 36921 | $0.03 \pm 0.02$ |          | $0.02 \pm 0.02$ |          | $0.02 \pm 0.00$ |          |         |
| 38150 | $0.14 \pm 0.03$ | 47       | $0.09 \pm 0.00$ | 50       | $0.13 \pm 0.02$ | 47       | BM      |
| 39578 | $0.12 \pm 0.01$ | 19       | $0.13 \pm 0.01$ | 23       | $0.13 \pm 0.02$ | 21       | S       |
| 40153 | $0.20 \pm 0.07$ | 59       | $0.20 \pm 0.02$ | 59       | $0.22 \pm 0.02$ | 61       | S       |
| 40692 | $0.11 \pm 0.01$ |          | $0.11 \pm 0.00$ |          | $0.11 \pm 0.00$ |          | S       |
| 41333 | $0.25 \pm 0.01$ | 73       | $0.25 \pm 0.01$ | 73       | $0.25 \pm 0.01$ | 73       | BM      |
| 41517 | $0.07 \pm 0.01$ |          | $0.07 \pm 0.00$ |          | $0.07 \pm 0.00$ |          |         |
| 42089 | $0.15 \pm 0.01$ | 61       | $0.14 \pm 0.01$ | 61       | $0.17 \pm 0.01$ | 59       | BM      |
| 42833 | $0.05 \pm 0.01$ | 17       | $0.05 \pm 0.01$ | 13       | $0.12 \pm 0.01$ | 19       | BM      |
| 42857 | $0.14 \pm 0.02$ |          | $0.14 \pm 0.00$ |          | $0.14 \pm 0.00$ |          | S       |
| 43186 | $0.03 \pm 0.01$ |          | $0.03 \pm 0.00$ |          | $0.04 \pm 0.02$ |          |         |
| 43321 | $0.04 \pm 0.01$ |          | $0.04 \pm 0.02$ |          | $0.04 \pm 0.01$ |          |         |
| 43495 | $0.02 \pm 0.01$ |          | $0.02 \pm 0.01$ |          | $0.02 \pm 0.01$ |          |         |
| 43671 | $0.21 \pm 0.00$ |          | $0.20 \pm 0.00$ |          | $0.20 \pm 0.01$ |          | B       |
| 44182 | $0.13 \pm 0.01$ |          | $0.12 \pm 0.00$ |          | $0.13 \pm 0.00$ |          |         |
| 45165 | $0.05 \pm 0.00$ |          | $0.04 \pm 0.02$ |          | $0.04 \pm 0.05$ |          |         |
| 45749 | $0.16 \pm 0.01$ | 25       | $0.15 \pm 0.01$ | 25       | $0.17 \pm 0.01$ | 28       | BM      |
| 45948 | $0.07 \pm 0.04$ |          | $0.04 \pm 0.03$ |          | $0.05 \pm 0.05$ |          |         |
| 46247 | $0.15 \pm 0.03$ | 45       | $0.16 \pm 0.04$ | 47       | $0.12 \pm 0.05$ | 45       | S       |
| 47404 | $0.16 \pm 0.00$ | 113      | $0.17 \pm 0.01$ | 113      | $0.17 \pm 0.00$ | 111      | S       |
| 48171 | $0.25 \pm 0.04$ | 50       | $0.27 \pm 0.02$ | 61       | $0.24 \pm 0.05$ | 61       | S       |
| 50063 | $0.10 \pm 0.02$ |          | $0.14 \pm 0.02$ |          | $0.15 \pm 0.02$ |          | S       |
| 55588 | $0.22 \pm 0.03$ | 13       | $0.21 \pm 0.00$ | 15       | $0.26 \pm 0.02$ | 15       | BM      |
| 56219 | $0.08 \pm 0.01$ |          | $0.09 \pm 0.04$ |          | $0.09 \pm 0.01$ |          |         |
| 61742 | $0.16 \pm 0.10$ |          | $0.20 \pm 0.01$ |          | $0.20 \pm 0.01$ |          | B       |
| 68096 | $0.05 \pm 0.01$ |          | $0.06 \pm 0.00$ |          | $0.05 \pm 0.00$ |          |         |
| 68165 | $0.01 \pm 0.01$ |          | $0.01 \pm 0.02$ |          | $0.02 \pm 0.00$ |          |         |
| 69253 | $0.27 \pm 0.04$ | 58       | $0.22 \pm 0.02$ | 50       | $0.22 \pm 0.03$ | 50       | BM      |
| 69327 | $0.14 \pm 0.03$ | 45       | $0.10 \pm 0.01$ | 33       | $0.11 \pm 0.01$ | 53       | S       |
| 71047 | $0.12 \pm 0.02$ |          | $0.07 \pm 0.01$ |          | $0.09 \pm 0.00$ |          |         |
| 72060 | $0.20 \pm 0.00$ | 13       | $0.23 \pm 0.00$ | 13       | $0.22 \pm 0.00$ | 13       | BM      |

S =  $Q_T$  due to spiral arms B = bar-like “butterfly” structure, but no clear  $Q_T$ -maximum in the assumed bar region BM= both  $Q_T$ -maximum and bar-like butterfly structure appear

**Table 4.** For the test galaxies: bar strengths and the parameters used in the calculation.

| Galaxy   | PA  | INC  | DIST [Mpc] | $Q_b(sech^2)$ | $Q_b(sech)$ | $Q_b(exp)$ | $Q_b(BB)$       |
|----------|-----|------|------------|---------------|-------------|------------|-----------------|
| Maffei2  | 23  | 65.1 | 3.4        | 0.33          | 0.34        | 0.35       | $0.27 \pm 0.03$ |
| E565-G11 | 73  | 33.0 | 63.0       | 0.39          | 0.41        | 0.42       | $0.28 \pm 0.03$ |
| E566-G24 | 67  | 42.5 | 45.0       | 0.36          | 0.37        | 0.39       | $0.27 \pm 0.04$ |
| N309     | 175 | 33.7 | 75.5       | 0.26          | 0.27        | 0.28       | $0.11 \pm 0.02$ |
| N1300    | 106 | 48.6 | 18.8       | 0.55          | 0.58        | 0.60       | $0.42 \pm 0.06$ |
| N1637    | 15  | 35.6 | 8.9        | 0.20          | 0.21        | 0.22       | $0.09 \pm 0.03$ |
| N2543    | 45  | 54.9 | 32.9       | 0.31          | 0.33        | 0.35       | $0.28 \pm 0.05$ |
| N3081    | 123 | 33.0 | 32.5       | 0.28          | 0.28        | 0.29       | $0.17 \pm 0.02$ |
| N4548    | 150 | 37.4 | 16.8       | 0.38          | 0.39        | 0.40       | $0.44 \pm 0.03$ |
| N4653    | 30  | 29.4 | 39.1       | 0.20          | 0.22        | 0.23       | $0.04 \pm 0.01$ |
| N5371    | 8   | 37.4 | 34.1       | 0.19          | 0.20        | 0.21       | $0.19 \pm 0.02$ |
| N5905    | 135 | 48.6 | 42.5       | 0.43          | 0.44        | 0.45       | $0.43 \pm 0.05$ |
| N7479    | 25  | 40.6 | 32.4       | 0.73          | 0.76        | 0.79       | $0.63 \pm 0.08$ |

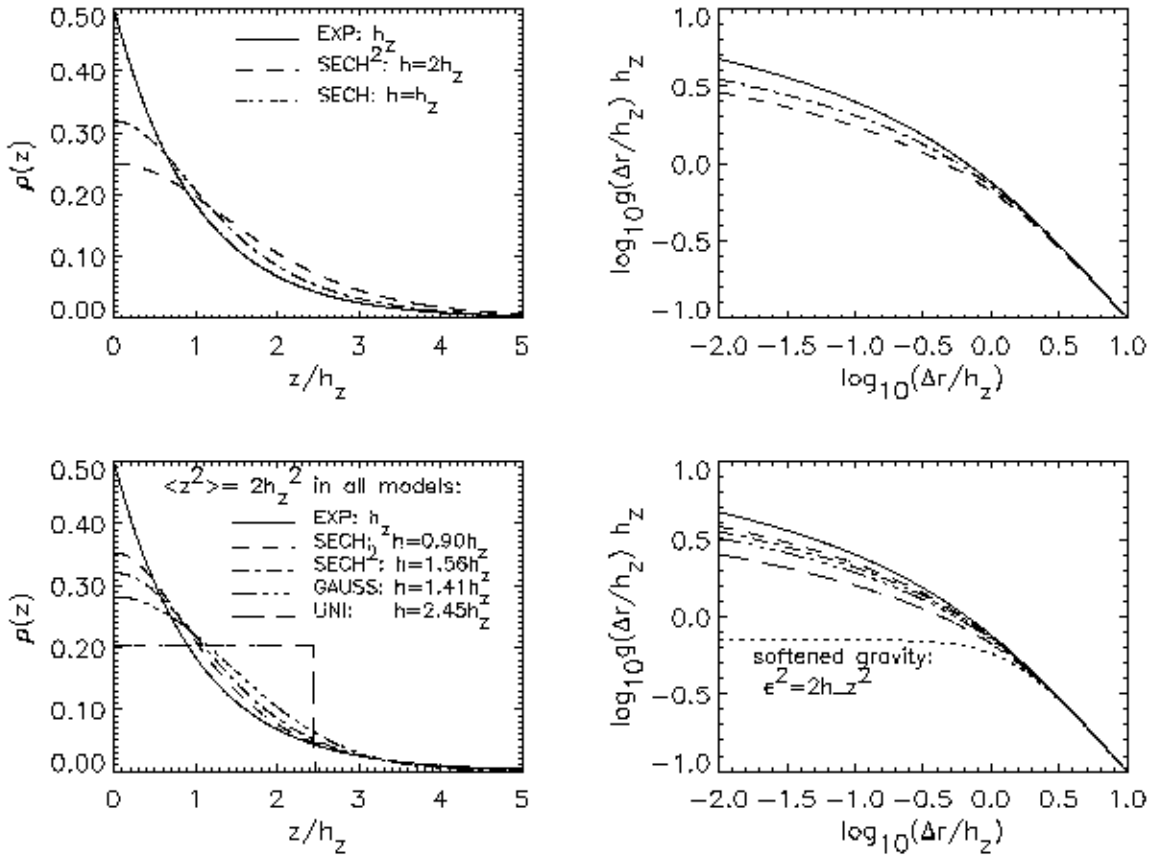


Fig. 1

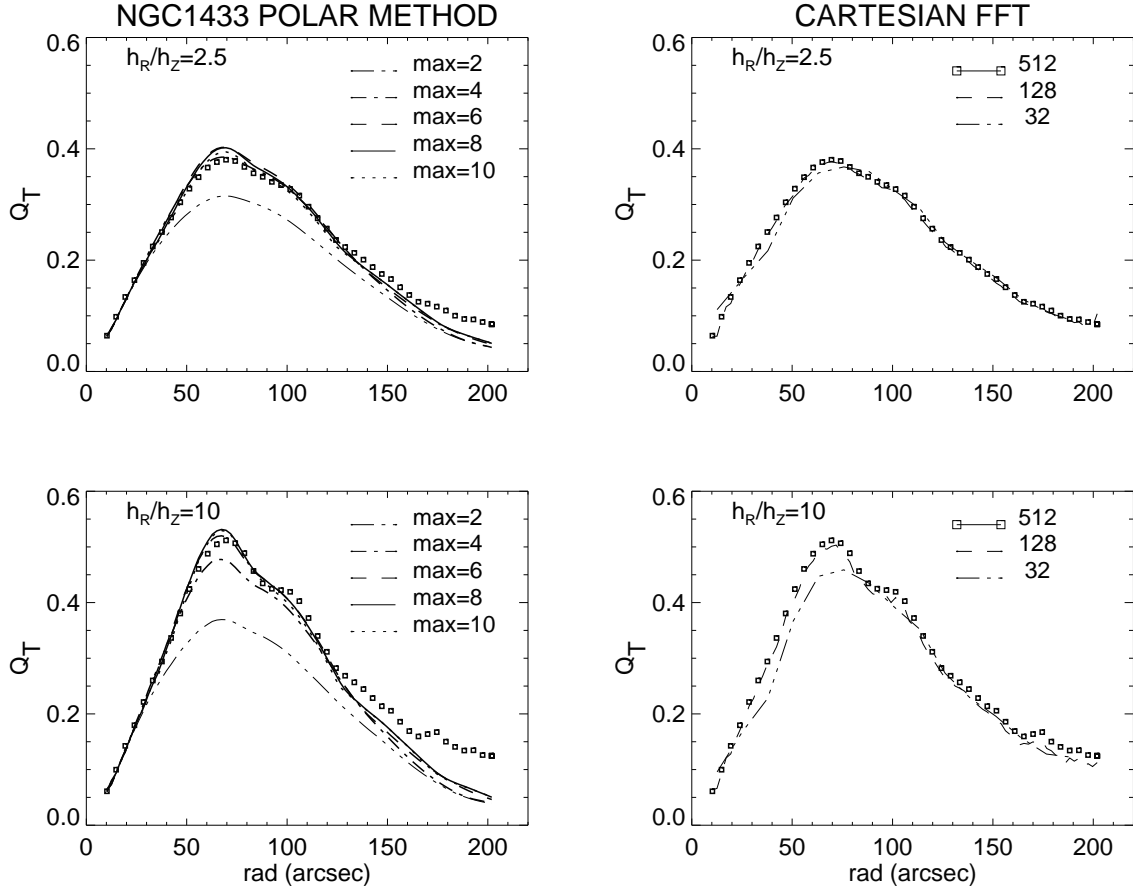


Fig. 2

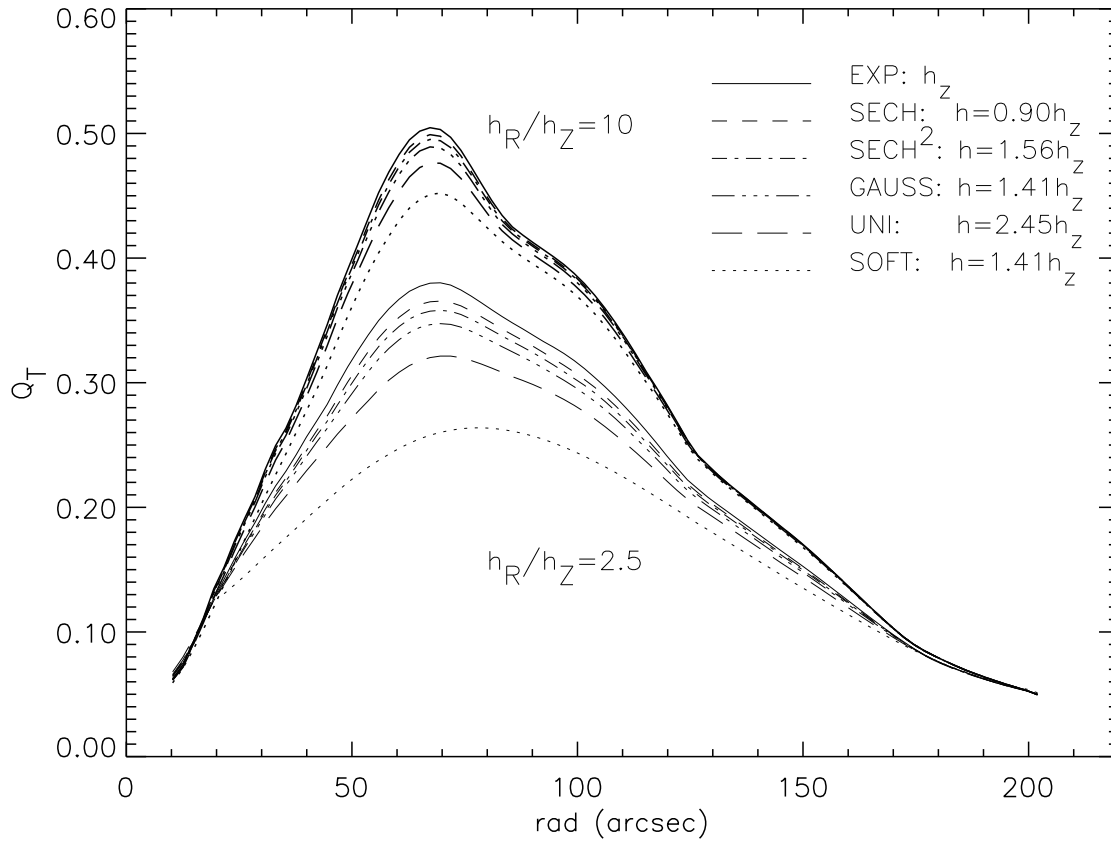


Fig. 3

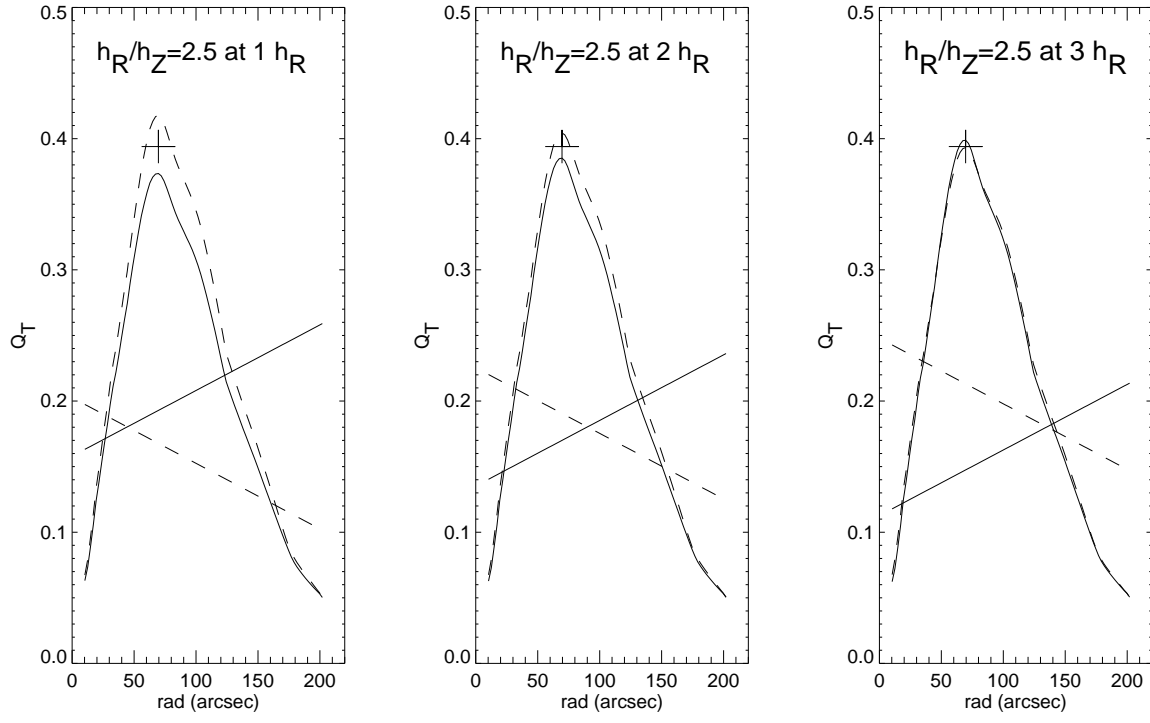


Fig. 4

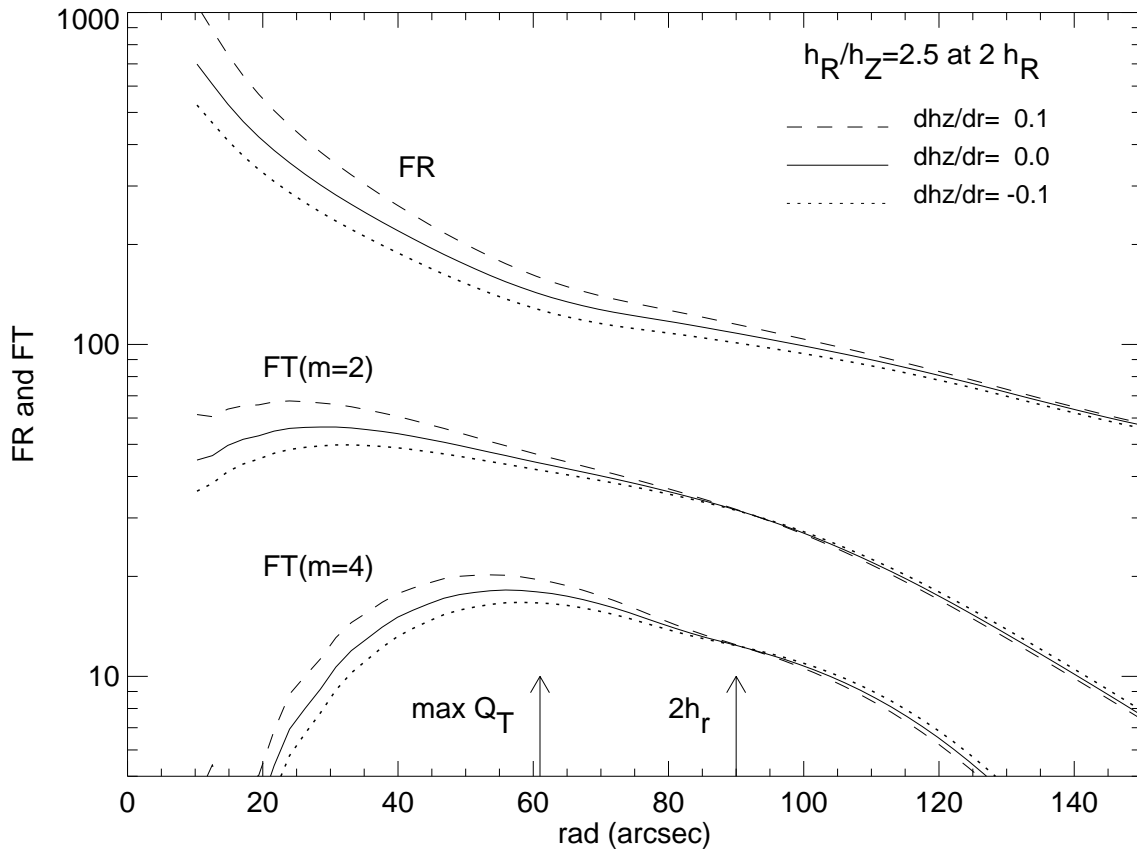


Fig. 5

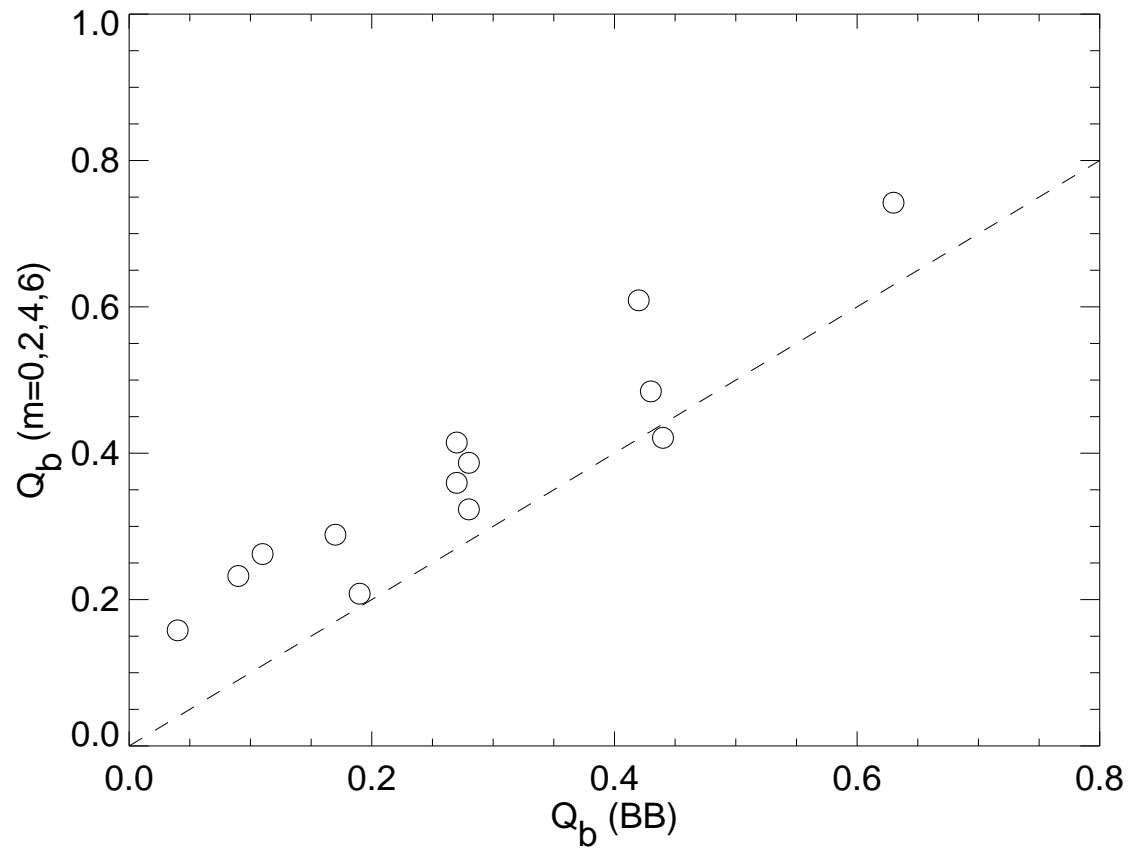


Fig. 6

logtest1.ps

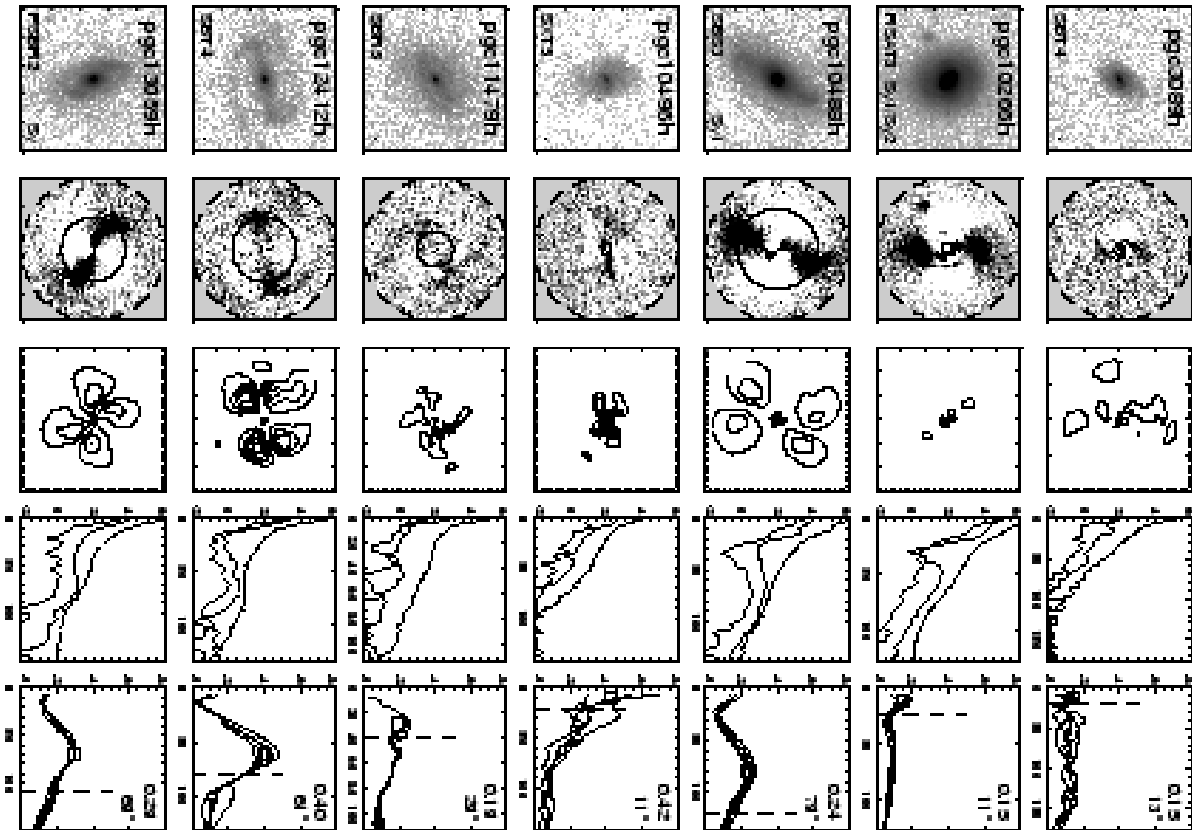


Fig. 7a



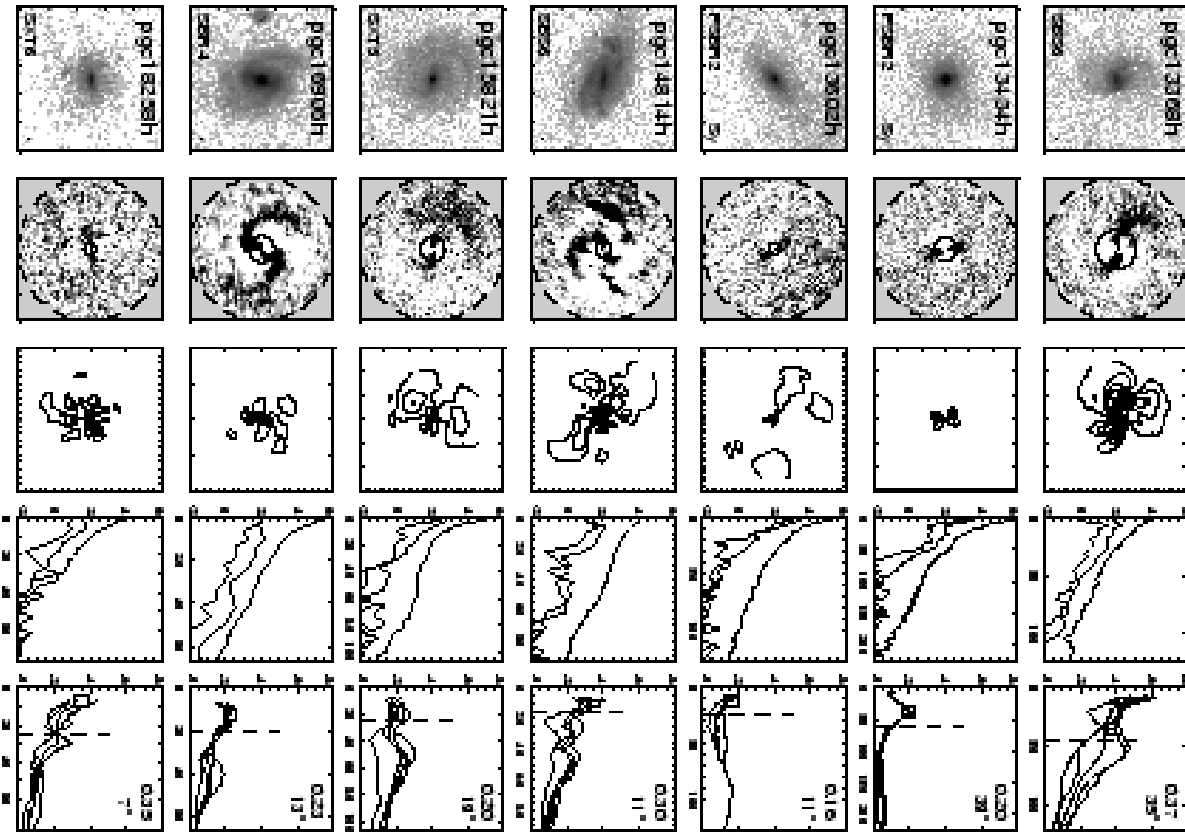


Fig. 7b

661ae13.ps

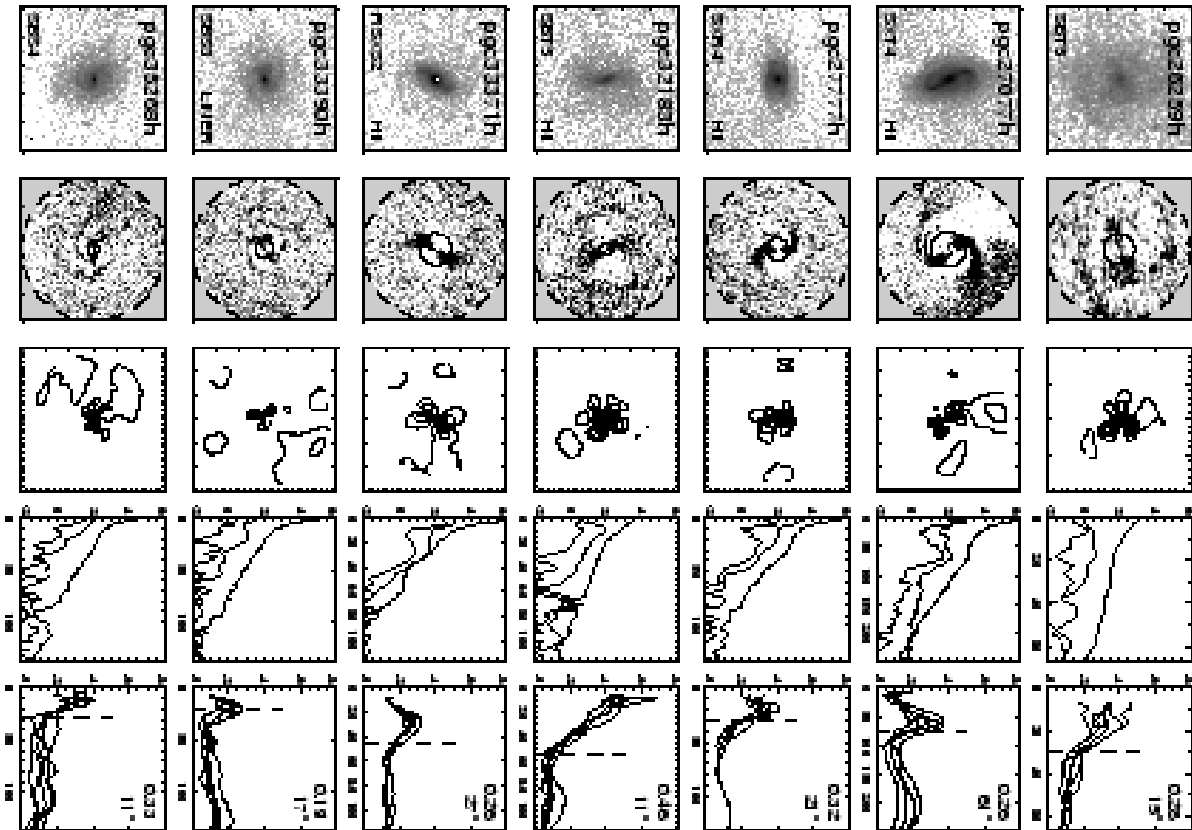


Fig. 7c

b61test4.ps

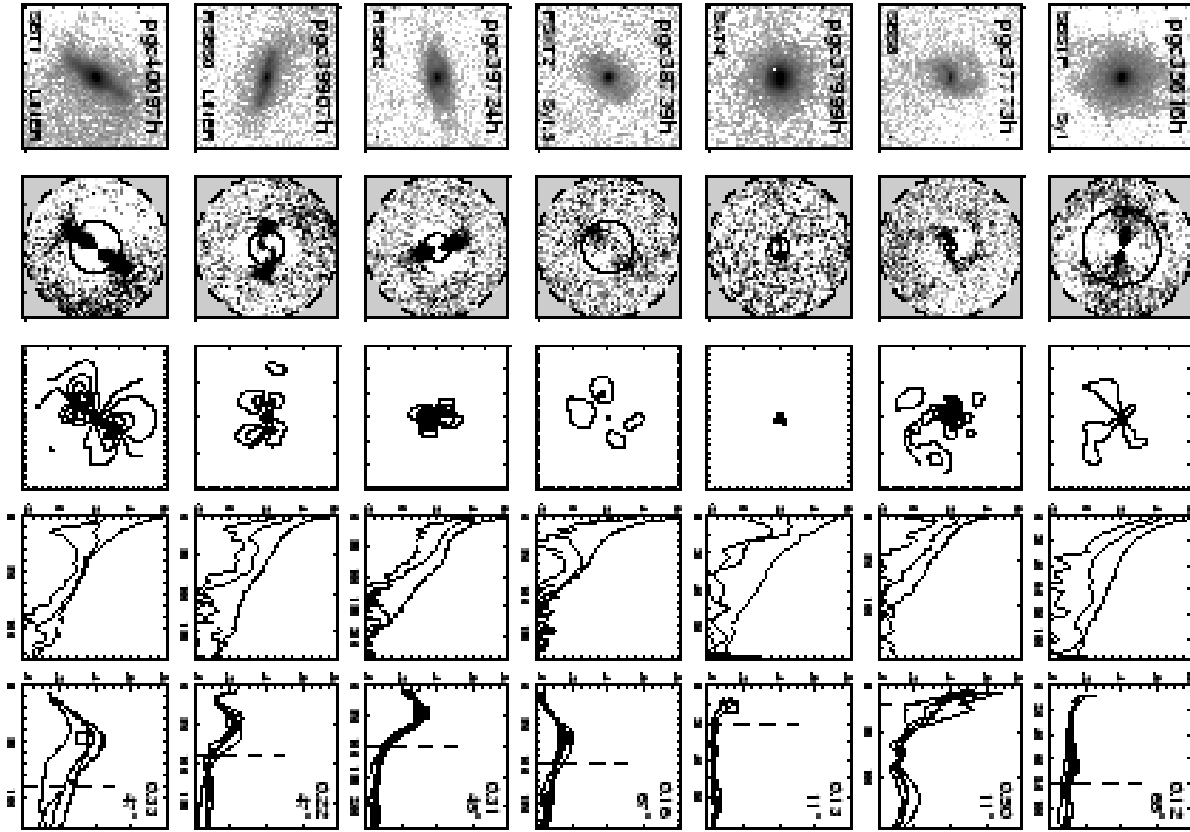


Fig. 7d

661ae15.ps

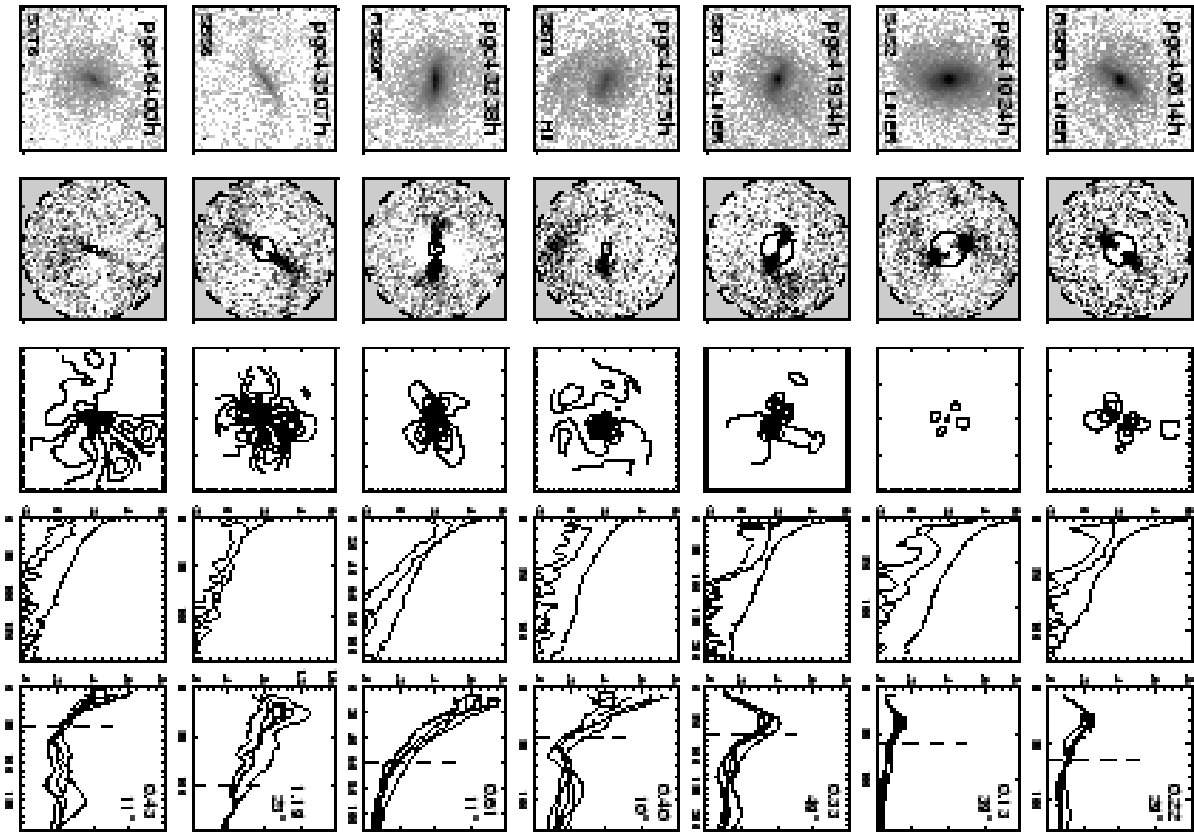


Fig. 7e

661test6.ps

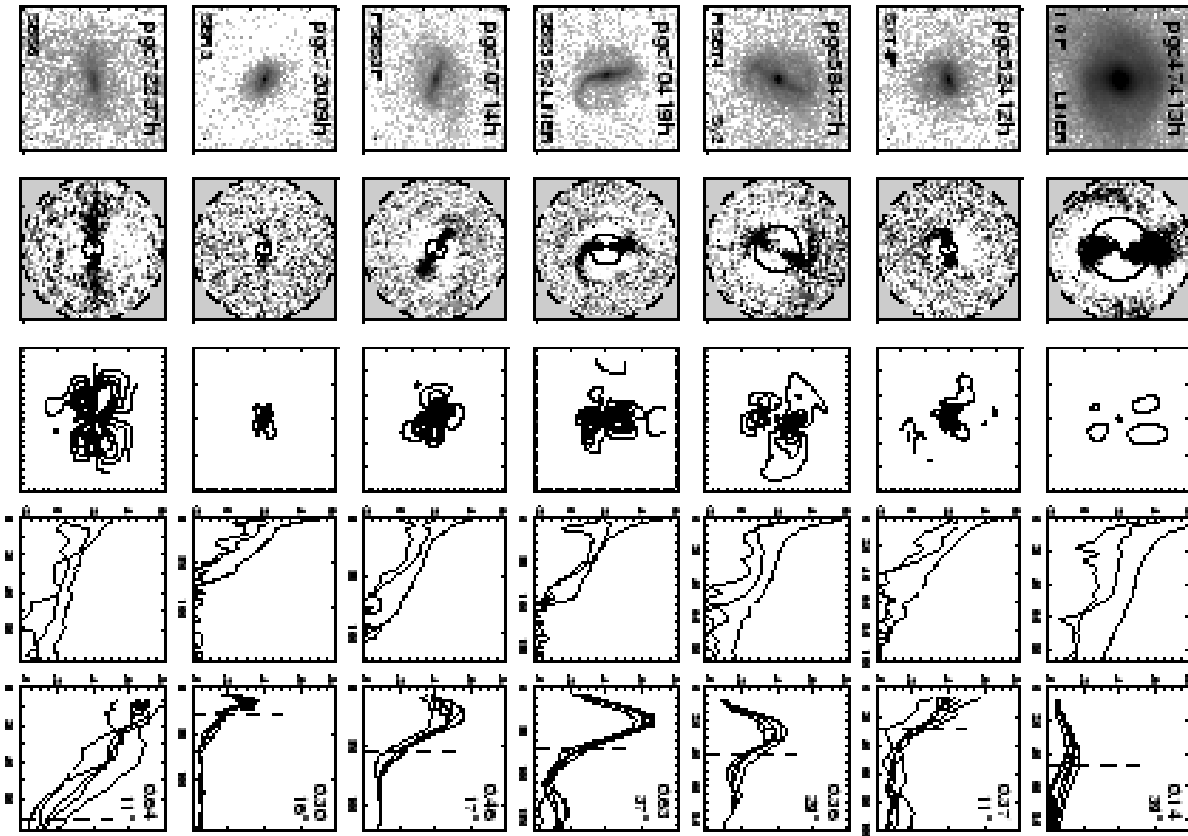


Fig. 7f

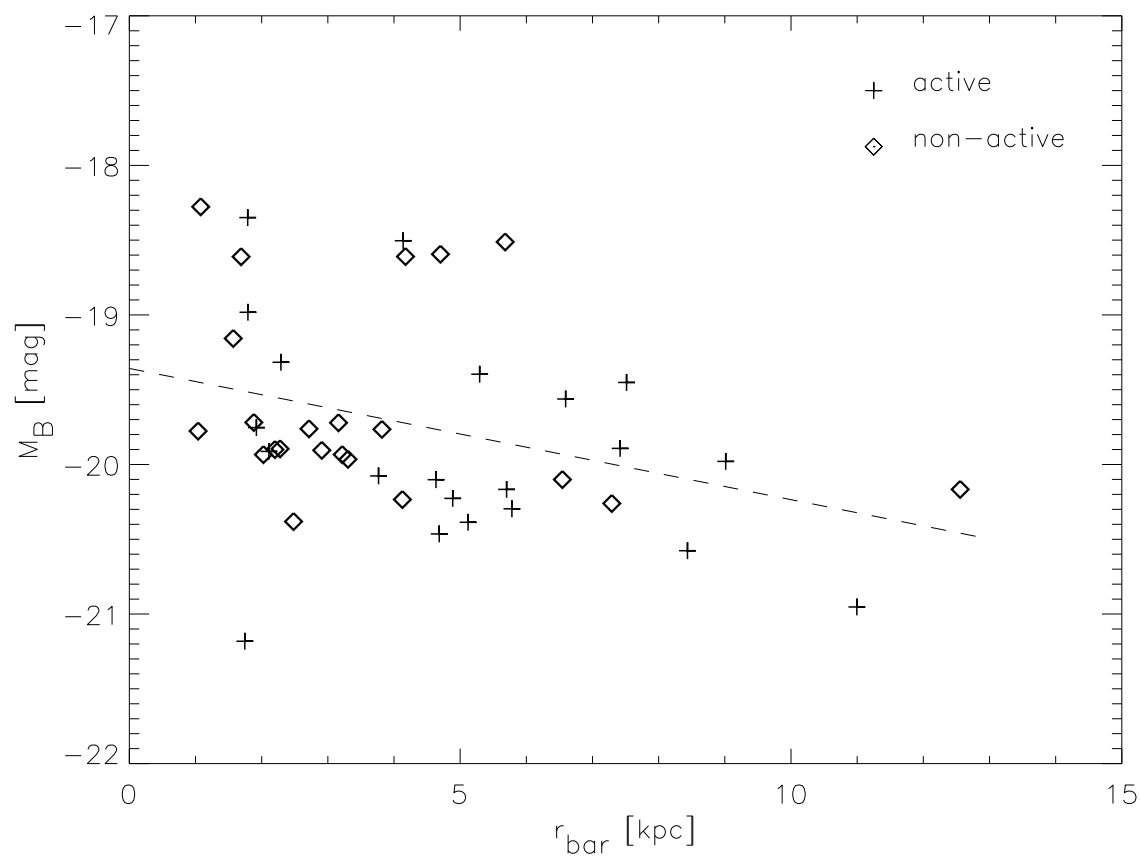


Fig. 8a

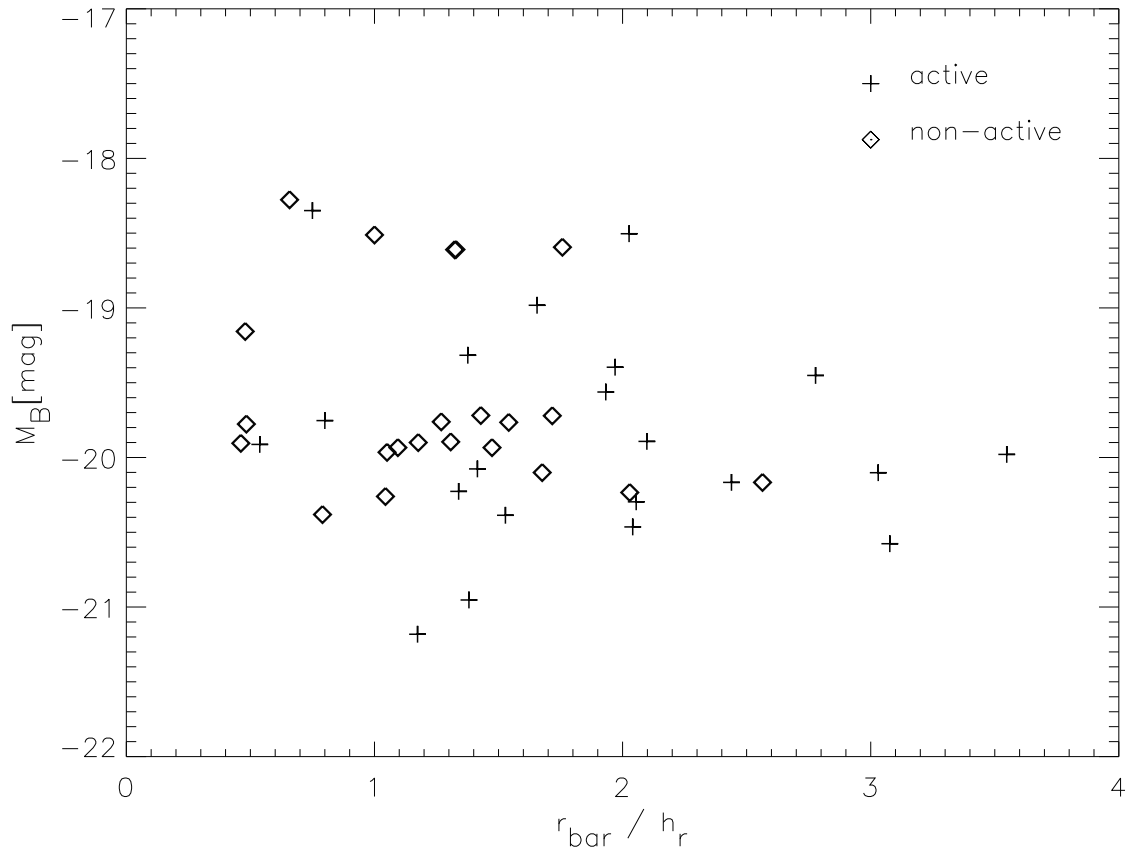


Fig. 8b

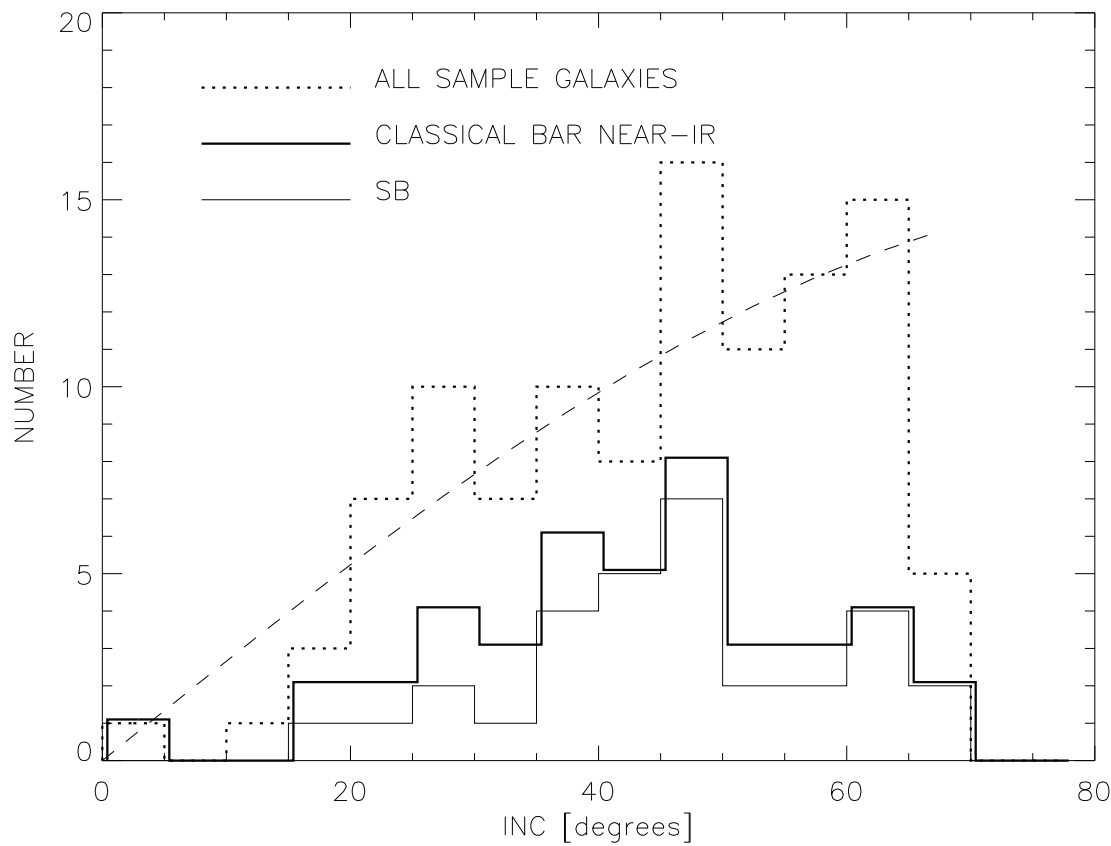


Fig. 9



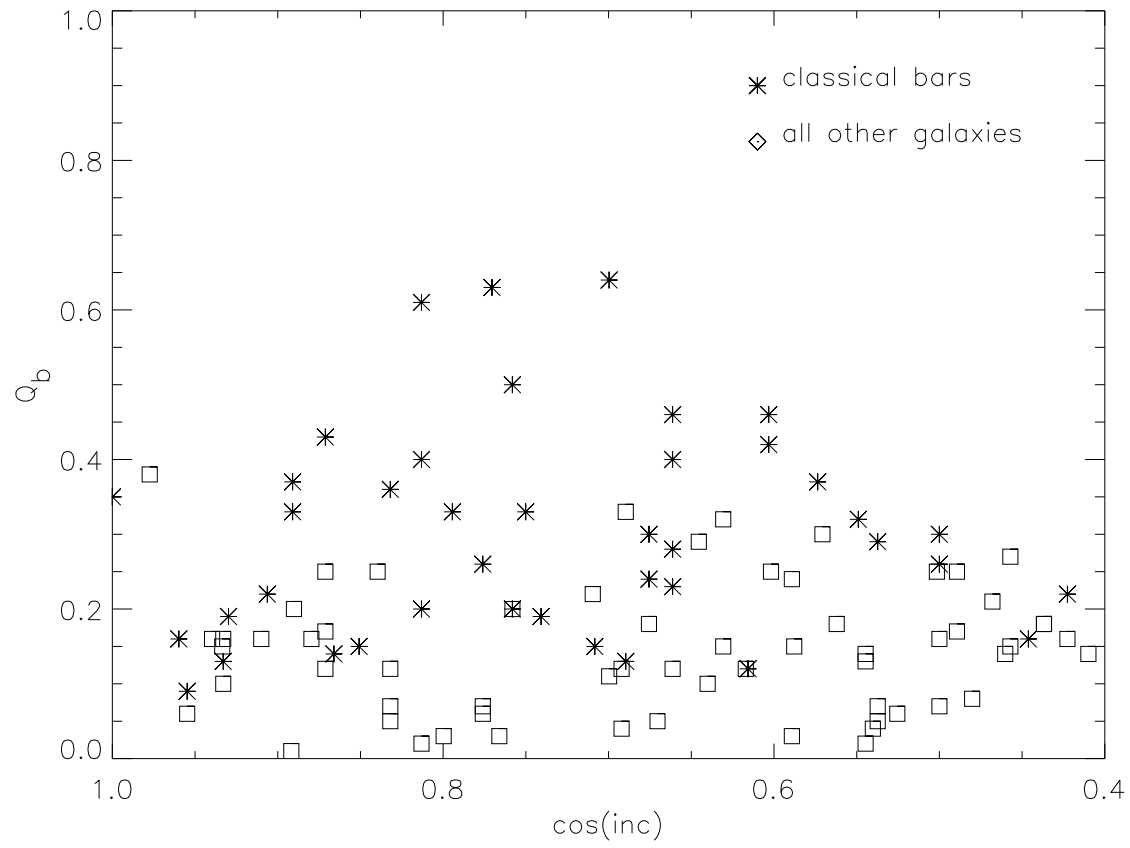


Fig. 10

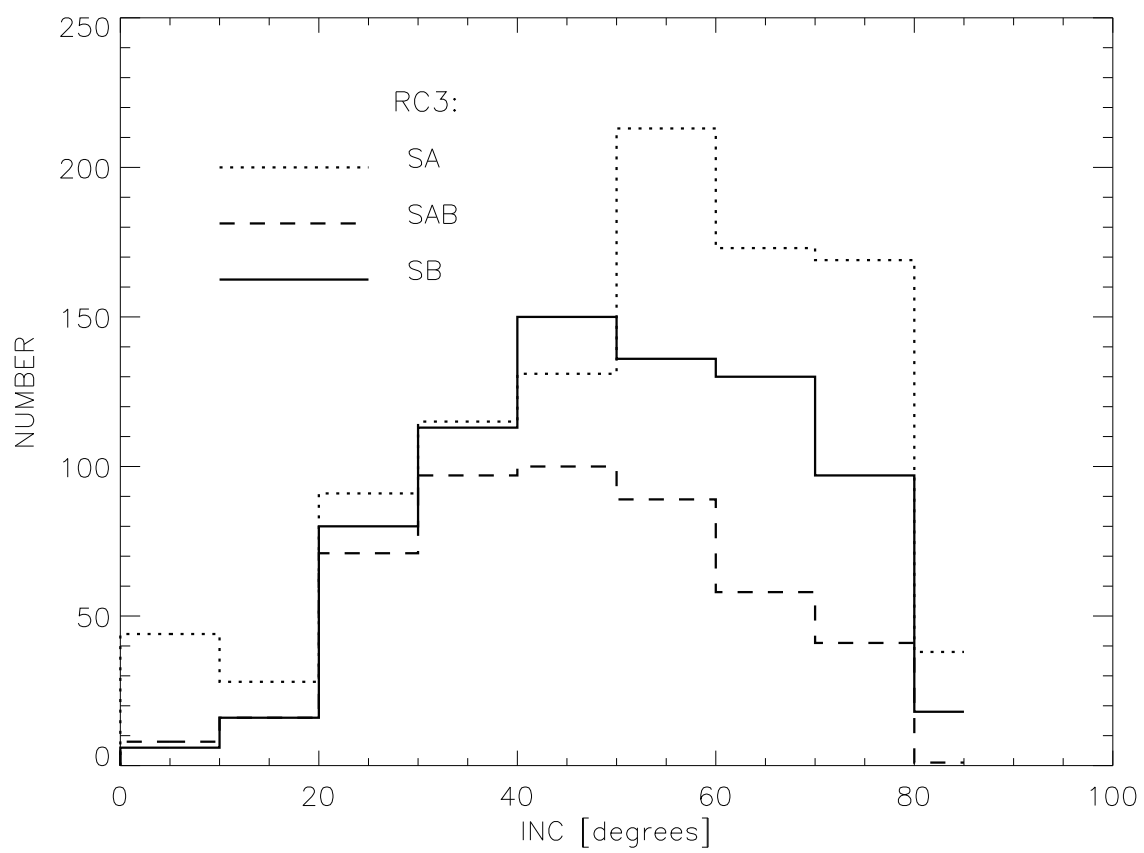
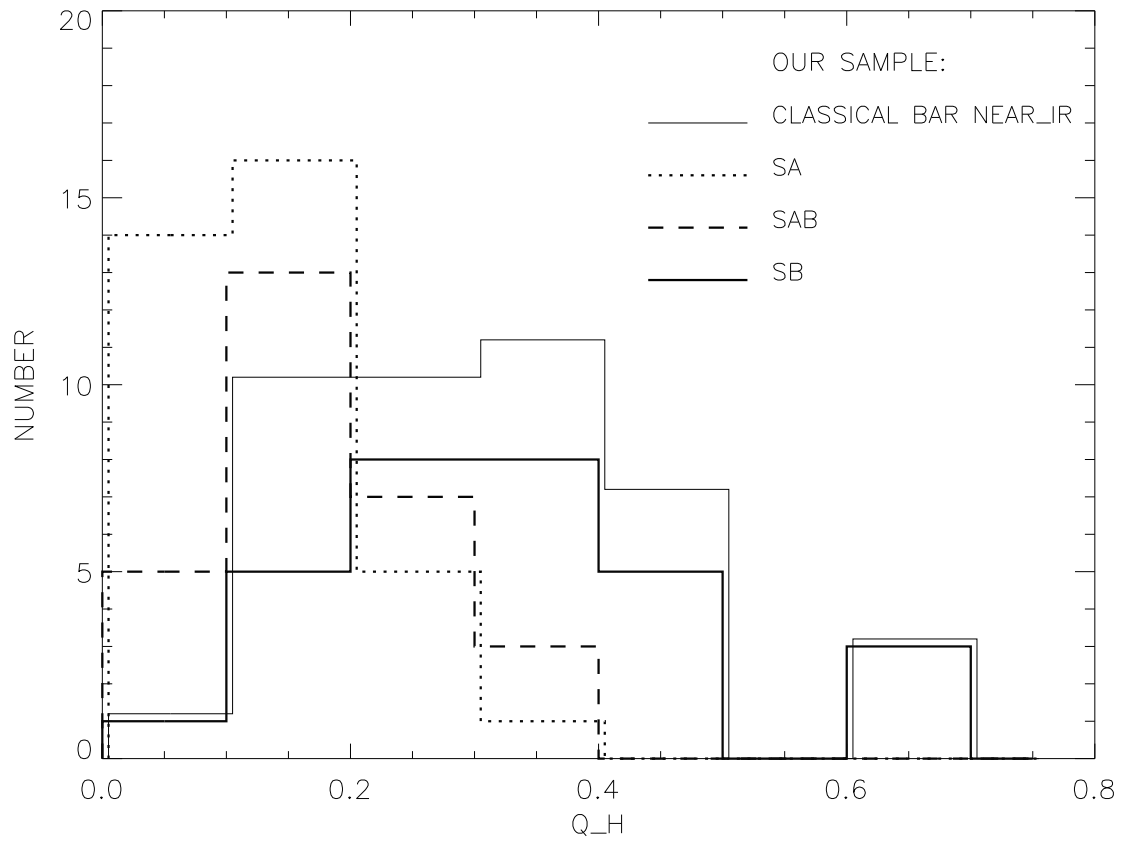


Fig. 11



10Fig. 12a

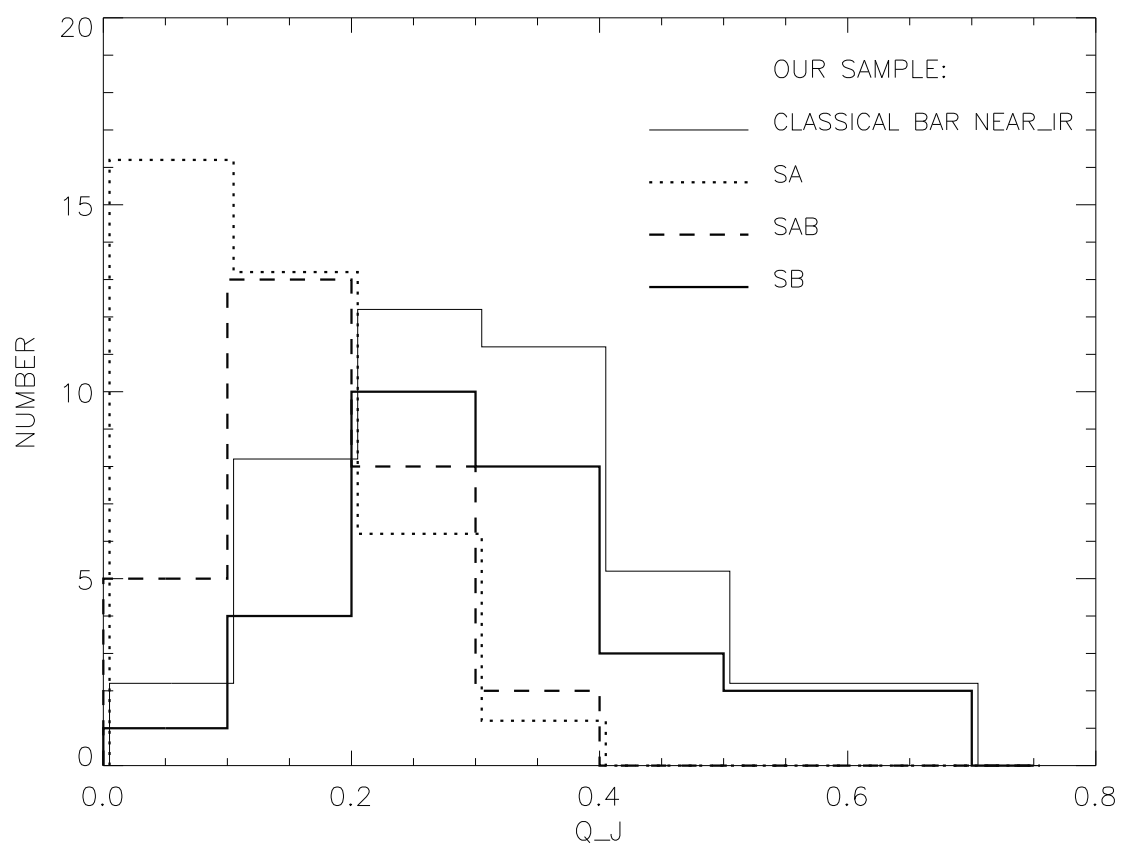


Fig. 12b

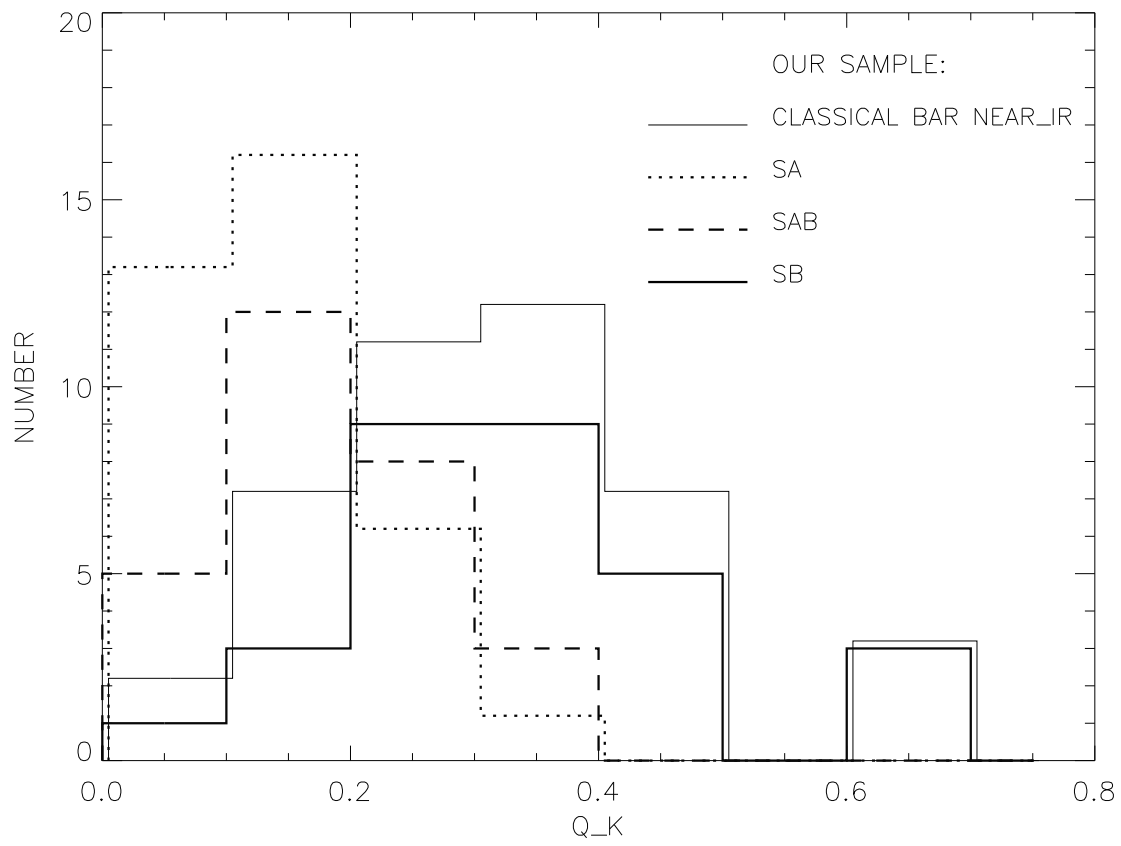


Fig. 12c

This paper has been produced using the Royal Astronomical Society/Blackwell Science T<sub>E</sub>X macros.